Article

Time-resolved structural analysis of an RNA-cleaving DNA catalyst

https://doi.org/10.1038/s41586-021-04225-4

Received: 29 May 2021

Accepted: 6 November 2021

Published online: 23 December 2021

Check for updates

Jan Borggräfe[1,2], Julian Victor[1], Hannah Rosenbach[1], Aldino Viegas[1,10], Christoph G. W. Gertzen[3,4], Christine Wuebben[5], Helena Kovacs[6], Mohanraj Gopalswamy[3], Detlev Riesner[1], Gerhard Steger[1], Olav Schiemann[5], Holger Gohlke[2,3,7], Ingrid Span[1,8] & Manuel Etzkorn[1,2,9]✉

The 10–23 DNAzyme is one of the most prominent catalytically active DNA sequences[1,2]. Its ability to cleave a wide range of RNA targets with high selectivity entails a substantial therapeutic and biotechnological potential[2]. However, the high expectations have not yet been met, a fact that coincides with the lack of high-resolution and time-resolved information about its mode of action[3]. Here we provide high-resolution NMR characterization of all apparent states of the prototypic 10–23 DNAzyme and present a comprehensive survey of the kinetics and dynamics of its catalytic function. The determined structure and identified metal-ion-binding sites of the precatalytic DNAzyme–RNA complex reveal that the basis of the DNA-mediated catalysis is an interplay among three factors: an unexpected, yet exciting molecular architecture; distinct conformational plasticity; and dynamic modulation by metal ions. We further identify previously hidden rate-limiting transient intermediate states in the DNA-mediated catalytic process via real-time NMR measurements. Using a rationally selected single-atom replacement, we could considerably enhance the performance of the DNAzyme, demonstrating that the acquired knowledge of the molecular structure, its plasticity and the occurrence of long-lived intermediate states constitutes a valuable starting point for the rational design of next-generation DNAzymes.

Biocatalysis is usually carried out by proteins (that is, enzymes) and catalytically active RNAs (that is, ribozymes). So far, no DNA catalyst has been found in nature. However, several different catalytically active single-stranded DNA sequences have been identified by in vitro selection and have been named DNAzymes. DNAzymes are capable of catalysing various chemical reactions serving different purposes[1,2,4–7].

RNA-cleaving DNAzymes carry a high therapeutic potential to target RNA-based viruses or to act as gene silencers in the large class of diseases linked to non-coding RNA or elevated expression levels of certain proteins. The prototypic RNA-cleaving DNAzyme comprises a catalytic core sequence flanked by two substrate-binding arms (Fig. 1a). While the core catalyses the RNA cleavage into two fragments, the arms can be designed to recognize a given target sequence with high selectivity.

Previous crystallographic studies revealed snapshots of the post-catalytic state of the RNA-ligating 9DB1 DNAzyme[8] and the RNA-cleaving 8–17 DNAzyme in the precatalytic complex with a biological inactive DNA target[9]. Yet, all catalytically relevant states of one of the most prominent RNA-cleaving DNAzymes, that is, the 10–23 DNAzyme (Dz)[1], have eluded attempts at high-resolution characterization.

In theory, DNAzyme-based therapeutic strategies display appealing inherent properties such as high selectivity, straightforward design, relatively small size, independence of protein cofactors, absence of permanent effects on the genome, and comparatively fast and cost-effective production. However, therapeutic success has been rare so far, which coincides with reduced catalytic activity in a cellular environment[2,10,11] as well as an insufficient mechanistic understanding. Development of in vitro and dedicated cellular applications based on randomized optimizations or systematic screenings has led to gradual progress over the past two decades[12–14]. Rational design strategies could potentially further promote the advances of the DNAzyme technology. However, to enable this pathway, it is instrumental to adequately understand the basis of the DNA-mediated catalysis process, including the underlying molecular structure, dynamic processes and transition states. Here we set out to provide a foundation for such strategies.

For our study, we chose a Dz that targets the mRNA that encodes prion protein[10]. In general, a palindromic sequence within the catalytic loop of Dz (Fig. 1a, grey) promotes the formation of catalytically inactive dimers, which obstructed previous crystallographic structural

[1]Institut für Physikalische Biologie, Heinrich Heine University Düsseldorf, Düsseldorf, Germany. [2]Institute of Biological Information Processing (IBI-7: Structural Biochemistry), Forschungszentrum Jülich, Jülich, Germany. [3]Institute for Pharmaceutical and Medicinal Chemistry, Heinrich Heine University Düsseldorf, Düsseldorf, Germany. [4]Center for Structural Studies (CSS), Heinrich Heine University Düsseldorf, Düsseldorf, Germany. [5]Institute of Physical and Theoretical Chemistry, University of Bonn, Bonn, Germany. [6]Bruker Switzerland AG, Fällanden, Switzerland. [7]John von Neumann Institute for Computing (NIC), Jülich Supercomputing Centre (JSC) and Institute of Bio- and Geosciences (IBG-4: Bioinformatics), Forschungszentrum Jülich, Jülich, Germany. [8]Department of Chemistry and Pharmacy, Bioinorganic Chemistry, Friedrich Alexander University Erlangen-Nürnberg, Erlangen, Germany. [9]Jülich Center for Structural Biology (JuStruct), Forschungszentrum Jülich, Jülich, Germany. [10]Present address: UCIBIO, Department of Chemistry, NOVA School of Science and Technology, Universidade Nova de Lisboa, Caparica, Portugal. ✉e-mail: manuel.etzkorn@hhu.de

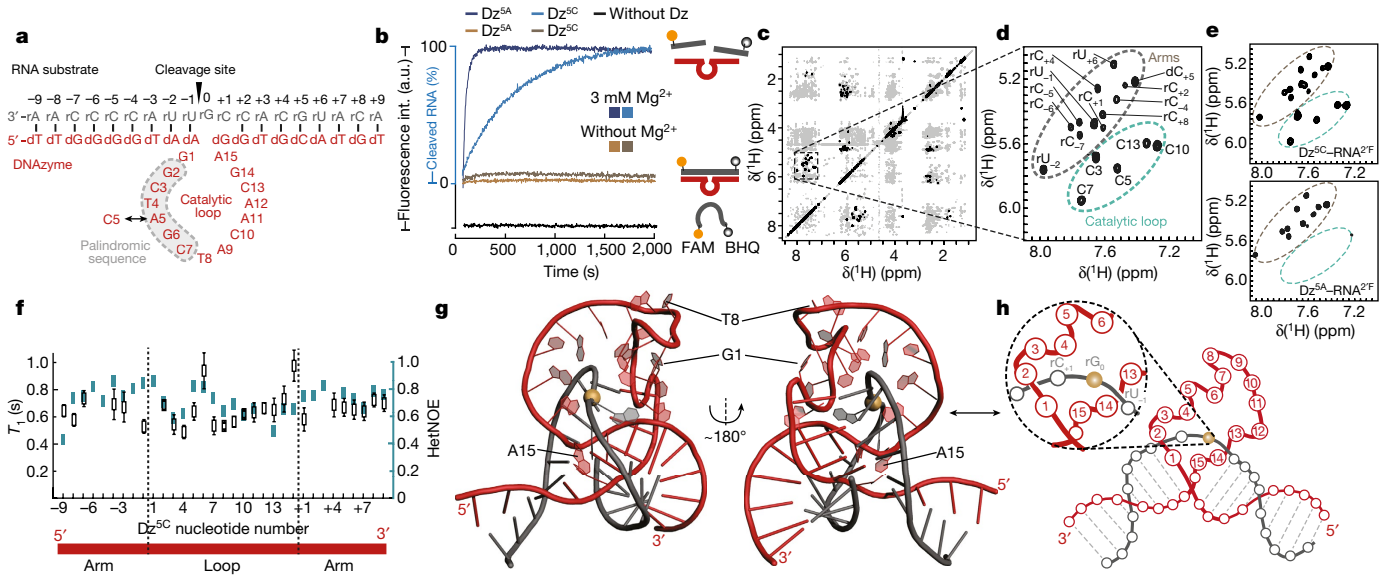

Fig. 1 | The precatalytic Dz–RNA complex adopts an unexpected but effective structure that is in dynamic exchange with divalent metal ions. **a**, Schematic overview of the used Dz targeting the mRNA encoding prion protein[10]. The Dz^{5C} variant breaks the palindrome of the conventional Dz^{5A} variant. **b**, FRET-detected single-turnover cleavage activity of the indicated Dz variants and conditions using a fluorophore (FAM)–quencher (BHQ) pair. **c**, Solution NMR ^{1}H–^{1}H correlations of Dz^{5C}–RNA$^{2'F}$ (TOCSY in black, and NOESY in grey) in the absence of divalent metal ions. **d**, Extract of the 'fingerprint' region focusing on pyrimidine H5–H6 correlations showing peak separation of the binding arms (grey dashed ellipse) and the catalytic loop (turquoise dashed ellipse). **e**, NMR fingerprint region of precatalytic complexes in the presence of 3 mM Mg^{2+} (corresponding to a molar ratio Mg^{2+}:Dz of 15) using variants Dz^{5C} (top) and Dz^{5A} (bottom). **f**, Nucleotide-specific dynamic measurements of the 1′-CH moieties in uniformly ^{13}C-labelled Dz (showing the fitted T_1 values ± standard error in black and calculated heteronuclear NOE (HetNOE) values in turquoise). **g**, Representative structure of the precatalytic Dz^{5C}–RNA$^{2'F}$ complex obtained from NMR-based ab initio calculation (representing cluster I; see main text, Methods and Extended Data Figs. 3–5 for more details). The golden sphere represents the phosphate of the scissile bond, Watson–Crick base pairings are shown as sticks, and non-base-paired nucleobases are shown as rings. Selected nucleotides are labelled for orientation. **h**, Simplified representation of the precatalytic complex highlighting the winding of the catalytic loop around the substrate.

studies[15]. Therefore, in addition to the original Dz^{5A} variant, we generated the variant Dz^{5C} that contains a substitution of adenine to cytosine in the fifth position of the catalytic loop, to break the palindrome. Both variants are fully active in the presence of Mg^{2+}, albeit at different rates ($k_{obs,\,3\,Mm\,MgCl_2} = 1.63 \times 10^{-3}\ s^{-1}$ and $1.71 \times 10^{-4}\ s^{-1}$ for Dz^{5A} and Dz^{5C}, respectively)[16] (Fig. 1b, Extended Data Fig. 1b). Yet, in the absence of divalent metal ions, stable precatalytic Dz–RNA complexes can be formed (Fig. 1b, brown). Alternatively, the RNA substrate can be protected from cleavage by introducing a 2′-fluorine substitution at position rG_0 (RNA$^{2'F}$) (Extended Data Fig. 1b).

The resulting precatalytic Dz–RNA$^{2'F}$ complex displays excellent NMR-spectral properties enabling near-complete resonance assignment of the 52-nucleotide complex, even without expensive ^{13}C and ^{15}N isotope enrichment (Fig. 1c, Extended Data Fig. 2). Particularly, the H5–H6 cross-correlations of pyrimidine nucleobases are clearly separated into the binding arm and catalytic loop regions, serving as a fingerprint of the respective state (Fig. 1d).

While the 2′F stabilization of the substrate (RNA$^{2'F}$) does not alter the overall structure of the precatalytic complex (Extended Data Fig. 1c, d), it enables investigation of the precatalytic complex in the presence of Mg^{2+} (Extended Data Fig. 1e). Since Mg^{2+} is required for activation (Fig. 1b), RNA$^{2'F}$ is a suitable substrate to study the desired precatalytic-activated Dz–RNA complex.

In contrast to the Dz^{5C} variant, the NMR fingerprint signals of all nucleotides in the catalytic loop of the Dz^{5A} variant disappear in the precatalytic-activated state (Fig. 1e). This behaviour is caused by Mg^{2+}-induced conformational exchange processes, whereas the faster exchange processes of the Dz^{5C} variant strongly facilitate NMR analysis (Extended Data Fig. 1e). Overall, the A5C mutation (1) eliminates the risk of dimerization associated with the palindromic sequence, (2) maintains activity, and (3) increases NMR accessibility. Consequently, in the following, we used the Dz^{5C}–RNA$^{2'F}$ complex in the presence of Mg^{2+} to unravel the molecular architecture of the 10–23 DNAzyme in the precatalytic-activated complex with its RNA substrate.

Structure of the precatalytic complex

The occurrence of amino peaks in the NMR spectra confirms the expected Watson–Crick hydrogen-bond formation for the binding arms, but does not reveal any stable amino group hydrogen-bond formation within the catalytic loop (Extended Data Fig. 3a). This observation raises the question about whether the Dz forms a defined complex structure at all, or whether a disordered catalytic loop only transiently converts into an active conformation. To answer this question, we investigated the dynamics of the Dz^{5C}–RNA$^{2'F}$ complex, expecting a disordered loop to display considerably enhanced dynamics. Using a uniformly ^{13}C-labelled Dz^{5C} construct in complex with unlabelled RNA$^{2'F}$, our NMR analysis consistently revealed that the loop does not exhibit substantially enhanced dynamics in the relevant fast time regime (Fig. 1f). These results indicate that the loop region is restrained, at least in part, to the rest of the precatalytic complex.

To characterize possible interactions, we exploited the denaturation behaviour of nucleic acid polymers using temperature-dependent NMR experiments (Extended Data Fig. 3b–d). The binding arms and cleavage site appear to be well restrained. By contrast, the catalytic loop only shows residual restraining in the 5′ side (C3–C7), whereas the 3′ side (T8–C13) probably comprises elevated levels of conformational plasticity.

We subsequently carried out a restraint-based structure calculation to obtain a high-resolution structure of defined regions and to narrow down the occupied conformational space of the regions that exhibited an increased conformational plasticity. In general, the

dilute proton network in nucleic acids impedes a structure determination solely based on semi-quantitative ^{1}H–^{1}H distances. Thus, to generate reliable structural information, we combined paramagnetic relaxation enhancements, conventional and exact nuclear Overhauser effects (NOEs)[17] with tailored novel approaches including homology restraining and ^{19}F-saturation transfer difference measurements (see Methods, Extended Data Figs. 3e–g, 4, Supplementary Fig. 1 for more details).

The obtained experimental restraints were loosely incorporated into a simulated annealing structure calculation to not force the ensemble into an over-restrained conformation, for two reasons: to our knowledge, no successful NMR-based structure determination of catalytic DNA serving as a reference has been reported so far, and the accuracy level of the new methodology is difficult to assess. Consequently, the overall root-mean-square deviation (RMSD) between the lowest-energy structures of the resulting structural ensemble remains moderately large (7–9 Å). The most prominent difference in the ensemble involves the relative orientation of the catalytic loop with respect to the binding arms. On the basis of this difference, the structures can be classified into four different clusters (Extended Data Figs. 3g, 5).

To evaluate the likelihood of each cluster, we determined residual dipolar couplings as reliable probes of relative molecular orientations (Extended Data Fig. 4j–m). Although spectral resolution and dispersion introduce limitations to this approach, the data clearly favour one specific fold. A fascinating feature of the obtained structure is a condensed core region involving an additional turn of the loop of Dz around the RNA (Fig. 1g, h, Supplementary Fig. 2). As a result of this unexpected molecular architecture, the substrate is locked in place and the cleavage site is fully exposed to the catalytic loop region.

Subsequent structure refinement and energy minimization resulted in a well-defined structural ensemble (RMSD around 3 Å; Extended Data Fig. 5c). To investigate whether the loosely restrained or refined ensemble better describes the conformational space of the precatalytic complex, we carried out multiple microsecond-long all-atom molecular dynamics (MD) simulations. Elevated root-mean-square fluctuations (RMSFs between 6 and 10 Å) for the catalytic loop region were consistently observed (Extended Data Fig. 6a, b). By contrast, the RMSFs of the nucleotides surrounding the substrate cleavage site are markedly lower (RMSF around 2.5 Å). These results reflect the structural variability observed in the loosely restrained annealing process (RMSDs of 6.2 and 2.6 Å for the loop and arm regions, respectively; Extended Data Fig. 6c).

In the following, we therefore focus on a representative of the loosely restrained ab initio calculation that captures key features of the experimental data instead of over-interpreting the obtained low-RMSD ensemble. We emphasize that the shown structure displays only one possible loop arrangement, which captures an interjacent conformation between the margins of the sampled conformational space of the ensemble that is generally characterized by increased conformational plasticity in the discussed loop region (Extended Data Fig. 6).

The role of metal ions

Divalent metal ions are established cofactors for Dz function[3]. Through a comprehensive characterization of Mg^{2+}, Mn^{2+} and $[Co(NH_3)_6]^{3+}$ interactions, we identify three binding sites for divalent metal ions with differential roles in regulating the catalytic activity of Dz (Fig. 2a, b, Extended Data Fig. 7).

Metal-ion-binding site I is located at the centre of a densely packed crossing of the binding arms, where it probably counteracts the resulting electrostatic repulsion of the phosphate backbones. The metal ion interactions indeed appear to considerably condense the structure (Fig. 2c). From the NMR structure, we identified two features promoting the structural condensation: (1) the *syn* conformation of the nucleotides at position −1 supporting the cleavage-site alignment, and (2) an out-of-register flip of dG_{+1} that breaks the expected Watson–Crick pairing and is a prerequisite for the unique passage of the loop through the otherwise double helix of the arms. NMR data analysis and a dedicated mutagenesis study corroborate these features (Extended Data Fig. 8a–g). As the observed behaviour distinctively aligns the catalytic loop and substrate, we refer to it as scaffolding.

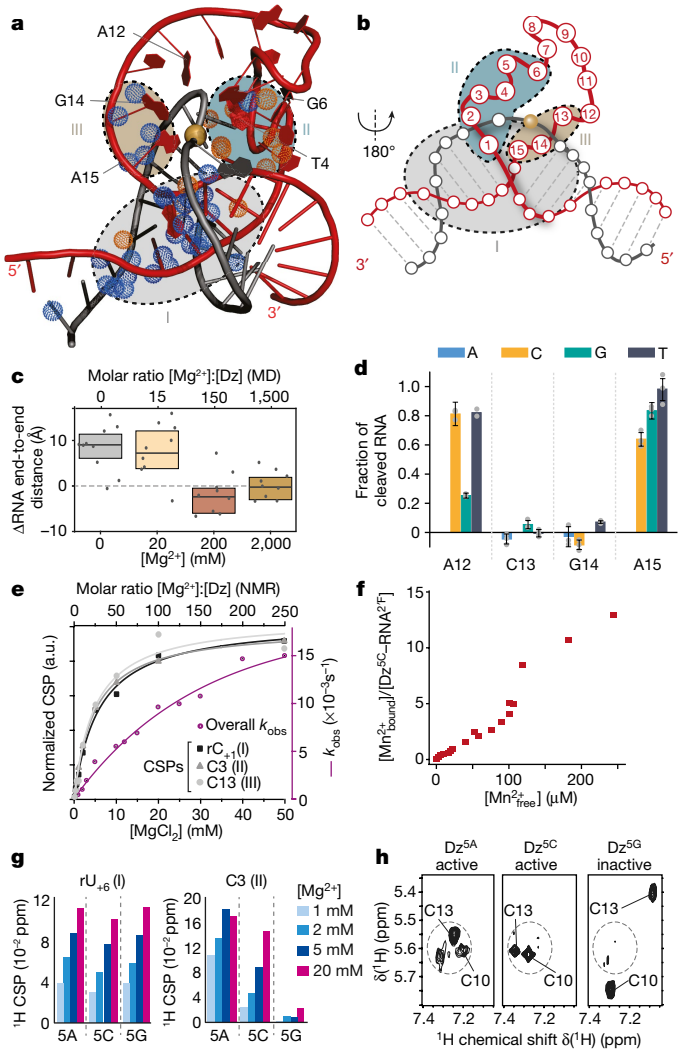

Fig. 2 | Metal-ion interactions determine the activity of Dz by condensing the structure and bringing the catalytic loop into an active conformation. **a**, Three distinct metal-ion-binding regions (labelled I–III) are identified when mapping the ^{1}H atoms most affected by the presence of Mg^{2+} (orange) or Mn^{2+} (blue) in NMR titrations. **b**, Simplified view on the metal-ion-binding regions. **c**, Box plot of the mean difference RNA end-to-end distance in MD simulations of the Dz^{5C}–RNA complex at different concentrations of Mg^{2+}. The difference to the refined starting structure is plotted, highlighting the Mg^{2+} dependence of complex condensation (centre line is the median, the box represents the 25–75% standard deviation, the dots are the individual data points from 10 independent replicas, and the dashed line provides the reference data for the starting structure). **d**, Changes in cleavage activity by mutations in the 3′ side of the catalytic loop. Data are presented as mean values ± standard deviation of triplicate experiments. **e**, Comparison of the Mg^{2+} dependency of the overall cleavage activity (k_{obs}, purple scale) and the induced structural modifications at the individual binding sites (chemical shift perturbations (CSPs), greyscale). **f**, EPR-derived Mn^{2+}-binding behaviour showing positive cooperative effects. **g**, Comparison of Mg^{2+}-induced CSPs of nucleotides in metal-ion-binding site I and site II in different Dz variants. **h**, NMR spectral extracts showing the effects of the indicated mutation at position 5 on sequentially distant nucleotides (C10 and C13).

Metal-ion-binding site II is associated with a metal-ion-induced conformational change in the 5′ side of the catalytic loop (Extended Data Fig. 7d, h), particularly promoting T4 as a conformational switch (Extended Data Figs. 3d, 8h, k). Although the scaffolding separates the involved nucleotides (positions 1–4) from the cleavage site, their importance for the activity of Dz was validated via a mutagenesis screen, which showed that 11 out of 12 possible single mutations are strongly detrimental for activity (Extended Data Fig. 8i). We therefore refer to the metal-ion-induced structural modifications in binding site II as conformational activation.

In MD simulations, we observed aromatic stacking between G6 of the catalytic loop and rG_0 in 18.4% of the time. These stacking interactions are twice as frequent when Mg^{2+} is bound to metal-ion-binding site II. In general, since aromatic stacking between purine bases is energetically more favourable over a broader range of twist angles[18], these data may provide a clue on the purine or pyrimidine preference of the cleavage site, the activating role of Mg^{2+} binding in metal-ion-binding site II, and the well-known importance of G6 in the catalytic loop[3].

Metal-ion-binding site III involves the 3′ side of the loop, which is brought close to the scissile bond via the scaffolding. The observed conformational plasticity can promote transient interactions of this loop region with the atoms involved in the catalysis reaction. In particular, C13, G14 and A15 show stronger interactions with divalent metal ions (Extended Data Fig. 7h). However, only the nucleobases of C13 and G14, but not A15, are essential for the activity (Fig. 2d), strongly suggesting a direct involvement of C13 and/or G14 in catalysis.

Notably, the structural effects of Mg^{2+} binding to each of the three binding sites are already saturated at considerably lower Mg^{2+} concentrations (Fig. 2e, chemical shift perturbation curves, greyscale) as the observed overall rate constants (Fig. 2e, k_{obs} curve, purple). This suggests that simultaneous occupation of multiple binding sites is required for substrate cleavage. To investigate possible cooperative effects, we characterized the interaction of metal ions from a Mn^{2+} point of view using electron paramagnetic resonance (EPR) spectroscopy[19]. The EPR spectra revealed a complex binding behaviour involving multiple binding sites with different affinities (Extended Data Fig. 8l–n, see Extended Data Fig. 7e for Mn^{2+}-induced activity). The binding curve shows positive cooperative behaviour for the binding sites with the highest Mn^{2+} affinities (Fig. 2f). Similar behaviour was also reported for the Dz^{5A} variant[10,20], pointing to the general notion that cooperative and coordinated metal ion interactions are a central element in the mode of action of Dz.

A comparative analysis of the Mg^{2+}-binding properties of the variants Dz^{5C}, Dz^{5A} and Dz^{5G} (a variant that contains a guanine in position 5 rendering the Dz inactive (Extended Data Fig. 8j)), revealed highly similar Mg^{2+} interactions in metal-ion-binding site I but pronounced differences in metal-ion-binding site II (Fig. 2g). These data directly connect the changes in the cleavage rates to a different Mg^{2+}-binding affinity of the adjoining metal-ion-binding site II. The inactivating A5G mutation, in contrast to the A5C mutation, also strongly affects the chemical environment of distant nucleotides, including metal-ion-binding site III (Fig. 2h), thus emphasizing a link between both metal-ion-binding sites. Overall, this corroborates the role of metal-ion-binding site II in Dz activation and further suggests that the central molecular architecture of the Dz^{5A} and Dz^{5C} variants, but not of the Dz^{5G} variant, is similar. In other words, and in line with the observed faster Mg^{2+} exchange rates (Extended Data Fig. 1e), the reduced activity of the Dz^{5C} variant probably originates from a less frequently populated metal-ion-binding site II, whereas the activity drop of the Dz^{5G} variant also involves larger structural modifications in the catalytic loop.

Mechanistic insights into the catalysis

To further understand the DNA-mediated catalysis and identify its limiting factors, we set out to characterize the additional states of Dz in the catalytic cycle. The central features of the respective states include a minimalistic fold of the single-stranded (free) Dz (state A in Fig. 3a, Extended Data Fig. 9a–d) and the auxiliary role of monovalent metal ions. The latter stabilize otherwise heterogenous complexes (states B_0, Extended Data Fig. 9a, e) and can partly mimic the effects of Mg^{2+}-induced scaffolding and conformational activation without promoting cleavage[20] (state B_1, Extended Data Fig. 9e–k). Our data imply that factors such as ineffective complex formation, misfolded single-stranded DNA or wrongly hybridized Dz–RNA complexes do not considerably restrict Dz activity. Consequently, the transition following the formation of homogenous precatalytic Dz–RNA complexes (state B_1 in Fig. 3a) appears to be most relevant to identify the limiting factors of catalysis.

The timescale of the Mg^{2+}-induced ensemble cleavage reaction (Fig. 1b) enables its investigation via time-resolved NMR spectroscopy. We exploited this opportunity by (1) encoding the kinetic information of the transition in the peak shape of a single 2D experiment[21], and (2) directly following the transition via a series of 1D ^{1}H spectra (Fig. 3b, Extended Data Fig. 10a–c). The spectra revealed that the substrate cleavage does not directly follow the Mg^{2+}-free state (Fig. 3c, black, state B_1) but occurs from an already Mg^{2+}-equilibrated state (Fig. 3c, blue, state B_2, Extended Data Fig. 10b). Accordingly, state B_2 can be considered a long-lived transient state, and thus a potential limiting factor of the catalytic cycle. The substrate cleavage is followed by an effective Mg^{2+} release (Extended Data Fig. 10c). Therefore, neither the Mg^{2+} turnover nor reaching the Mg^{2+} interaction equilibrium are rate-limiting steps of the catalysis.

The end point of the monitored reaction consists of at least two conformations (states C_1 and C_2) comprising DNAzymes that are still bound to the cleaved RNA (Extended Data Fig. 9a, l). These post-catalytic complexes display a destabilized core region and probably undergo slow conformational exchange processes (Extended Data Fig. 9m, o). While state C_1 is the dominant state at 37 °C, state C_2 is favoured at increasing temperatures just before complex dissociation (Extended Data Fig. 9n). Therefore, we named state C_2 'high entropy post-catalytic complex'.

To extract site-resolved kinetic information from the peak-shape distortions encoded in the 2D real-time spectrum, we developed a comprehensive analysis strategy that progresses previous studies[21,22] (Extended Data Fig. 10g–j). The resulting atomic-resolution insights into the cleavage kinetics reveal nuclear spins that experience either a slower or an elevated transition rate. Notably, the faster rates are exclusively found for atoms surrounding the cleavage site (Fig. 3d), pointing to the occurrence of a transient intermediate state comprising cleaved substrate but still an 'activated precatalytic-like' structure (state C_0 in Fig. 3a, see Supplementary Discussion for more details). Figure 3e shows the occurrence and kinetics of all discovered states during the cleavage reaction that are most consistent with our data.

Overall, it can be anticipated that optimization of Dz for in vivo applications will require dedicated modifications in all three metal-binding sites to overcome factors such as the strong dependency of the scaffolding and activation behaviour on metal ions (see Supplementary Discussion for more details). While this is beyond the scope of this study, we still explored the applicability of our newly generated insights into the structure, dynamics and occurrence of limiting transition states to increase the performance of Dz. In this respect, targeting the long-lived states B_2 and C_0, which already passed scaffolding and activation, appears promising. We speculate that the molecular plasticity of metal-binding site III allows interactions of different functional groups, particularly of G14, in different conformations associated with different catalytic rates.

During the MD simulations, G14 indeed interacted with the O2′ of rG_0 12.5% of the time, which is about fivefold more frequent than direct interactions of hydrated Mg^{2+} with this O2′, and no bridging of G14 and O2′ by Mg^{2+} was observed. Additional or subsequent interactions of hexa-hydrated Mg^{2+} or G14 with O5′ of rU_{-1} occur 5.9% or 6.8% of the time, respectively (Extended Data Fig. 10k).

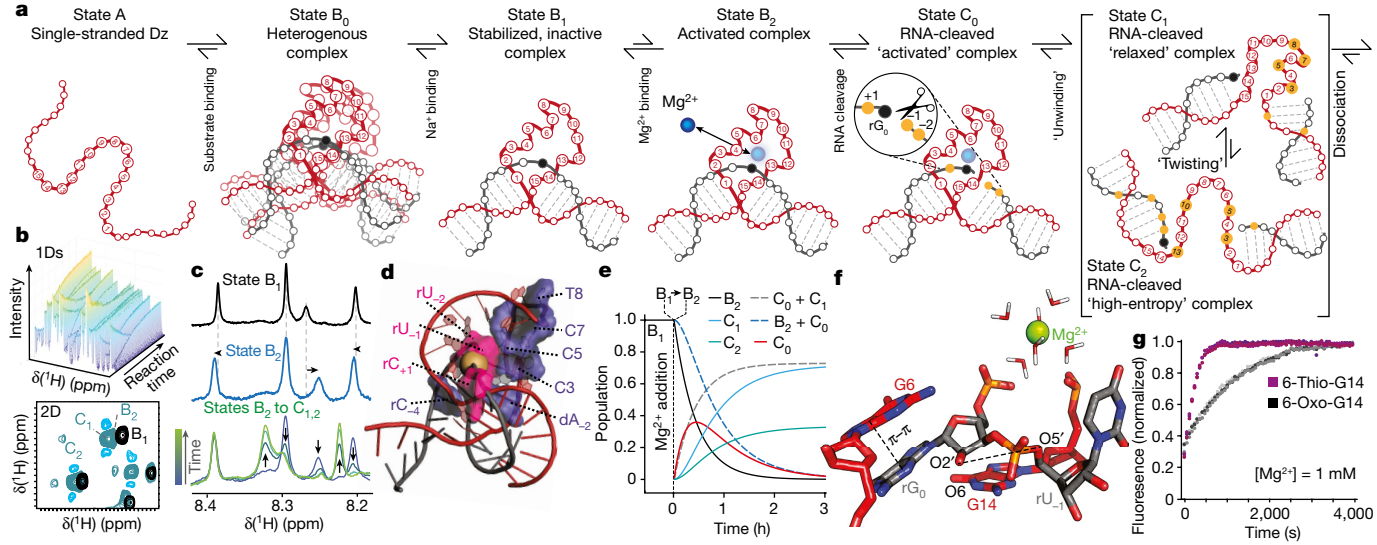

Fig. 3 | The catalytic reaction involves multiple rate-limiting transient intermediate states that offer suitable targets to increase the activity of Dz. **a**, Schematic of states occurring during the cleavage transition. Note that for simplicity the states are shown in a consecutive manner that reflects the experimental design and that under commonly applied conditions the states will form a dynamic equilibrium in the direction of the indicated arrows. Resolved and affected nucleotides reporting on changes in respect to the previous state are highlighted in orange for all C-states. **b**, Exemplary real-time NMR data recorded during the ensemble cleavage reaction (see Extended Data Fig. 10a–j for more details). **c**, Spectral extracts of 1D real-time NMR data recorded directly after Mg^{2+} addition (blue) and at subsequent time points (bottom). A spectrum before the addition of Mg^{2+} (black) serves as a reference. Horizontal and vertical black arrows indicate Mg^{2+}-induced CSPs and time-dependent changes in signal intensity, respectively. **d**, Location of nucleotides experiencing fast (magenta) and slow (purple) transition rates. Note that the magenta and purple regions correspond to the nucleotides highlighted in **a** for state C_0 and state C_1, respectively. **e**, Most plausible occurrence and kinetics of states involved in the cleavage reaction. The dashed lines represent experimentally observed mixed states for NMR detection (blue and grey). **f**, Snapshot taken from MD simulations showing a plausible cleavage mechanism involving the interaction of G14 with the O2′atom of rG_0, which is in the in-line attack conformation (dashed line) with P and O5′of rU_{-1}. A hexa-hydrated Mg^{2+} is in proximity to O5′. rG_0 engages in π-stacking interactions with G6. **g**, Rationally selected 6-thio-G14 modification considerably increases activity in the presence of Mg^{2+} (triplicate data points of FRET-based assays recorded in the presence of 1 mM Mg^{2+} are overlaid for each condition).

This points to an acid–base mechanism analogous to the 8–17 DNAzyme, where a functional group of a nucleotide acts as Brønsted base that abstracts a proton from the O2′, and a metal-ion-coordinated water molecule transfers a proton to the O5′while an in-line attack occurs[9]. This in-line attack (angle between O2′of rG_0, and P and O5′of rU_{-1} close to 180°) was found 3.3% of the time in our MD simulations and more frequently if Mg^{2+} was present in metal-binding site II (Extended Data Fig. 10l). The interaction between G14 and O2′and the in-line attack conformation (Fig. 3f) occur simultaneously during 0.8% of the time in MD simulations (Extended Data Fig. 10k), which may be related to the still low catalytic activity of Dz, as compared to protein-based catalysts. In this regard, Mg^{2+} binding to G14 could sterically hinder the interaction with rG_0 O2′and reduce the electron density in the purine ring, lowering the basicity of G14.

A 6-thio modification of G14 offers the opportunity to reduce these potentially catalytically detrimental Mg^{2+} interactions. In general, the substitution of oxygen by sulfur in 6-thio-dG lowers the basicity and strongly decreases Mg^{2+} affinity while still maintaining interactions with Mn^{2+}. The 6-thio-G14 modification indeed leads to an about sixfold increased cleavage rate in the presence of Mg^{2+} (Fig. 3g, $k_{obs,\,1\,mM\,MgCl_2} = 7.32 \times 10^{-4}\,s^{-1}$ and $4.16 \times 10^{-3}\,s^{-1}$ for oxo-G14 and thio-G14, respectively). By contrast, decreased rates are observed in the presence of Mn^{2+} (Extended Data Fig. 10m). This behaviour strongly differs from a 6-thio modification at position G6 used as a control[23] and is in line with an acid–base mechanism involving the nucleobase of G14 that competes with catalytically unfavourable Mg^{2+} interactions of the 6-oxo group of G14. Our data indicate that reducing these Mg^{2+} interactions via a 6-thio modification even outweighs the effects of the associated lowered pK_a.

In conclusion, our work highlights an intricate interplay between a unique molecular architecture, conformational plasticity and dynamic modulation by metal ions as the origin of the catalytic capabilities of DNA. Since the identified key features restrict access by most structural biology techniques, it is not surprising that this intriguing system evaded high-resolution characterization for decades and that suitable methods capable of capturing dynamic aspects are essential to draw an adequate picture of DNA catalysts. With the here presented atomic-level and time-resolved mechanistic description of one of the most potent RNA-cleaving DNAzyme, we aim to initiate the knowledge-based development of further enhanced next-generation DNAzymes. By successfully targeting the newly identified transient states and molecular plasticity of Dz, we provide initial proof of feasibility for such rational design strategies.

Online content

Any methods, additional references, Nature Research reporting summaries, source data, extended data, supplementary information, acknowledgements, peer review information; details of author contributions and competing interests; and statements of data and code availability are available at https://doi.org/10.1038/s41586-021-04225-4.

1. Santoro, S. W. & Joyce, G. F. A general purpose RNA-cleaving DNA enzyme. *Proc. Natl Acad. Sci. USA* **94**, 4262–4266 (1997).
2. Silverman, S. K. Catalytic DNA: scope, applications, and biochemistry of deoxyribozymes. *Trends Biochem. Sci* **41**, 595–609 (2016).
3. Rosenbach, H. et al. Molecular features and metal ions that influence 10-23 DNAzyme activity. *Molecules* **25**, 3100 (2020).
4. Cuenoud, B. & Szostak, J. W. A DNA metalloenzyme with DNA ligase activity. *Nature* **375**, 611–614 (1995).
5. Pradeepkumar, P. I., Höbartner, C., Baum, D. A. & Silverman, S. K. DNA-catalyzed formation of nucleopeptide linkages. *Angew. Chemie Int. Ed.* **47**, 1753–1757 (2008).

6. Shen, Z. et al. A catalytic DNA activated by a specific strain of bacterial pathogen. *Angew. Chemie Int. Ed.* **55**, 2431–2434 (2016).
7. Torabi, S.-F. et al. In vitro selection of a sodium-specific DNAzyme and its application in intracellular sensing. *Proc. Natl Acad. Sci. USA* **112**, 5903–5908 (2015).
8. Ponce-Salvatierra, A., Wawrzyniak-Turek, K., Steuerwald, U., Höbartner, C. & Pena, V. Crystal structure of a DNA catalyst. *Nature* **529**, 231–234 (2016).
9. Liu, H. et al. Crystal structure of an RNA-cleaving DNAzyme. *Nat. Commun.* **8**, 2006 (2017).
10. Victor, J., Steger, G. & Riesner, D. Inability of DNAzymes to cleave RNA in vivo is due to limited Mg^{2+} concentration in cells. *Eur. Biophys. J.* **47**, 333–343 (2018).
11. Young, D. D., Lively, M. O. & Deiters, A. Activation and deactivation of DNAzyme and antisense function with light for the photochemical regulation of gene expression in mammalian cells. *J. Am. Chem. Soc.* **132**, 6183–6193 (2010).
12. Wang, Y., Nguyen, K., Spitale, R. C. & Chaput, J. C. A biologically stable DNAzyme that efficiently silences gene expression in cells. *Nat. Chem.* **13**, 319–326 (2021).
13. Liu, C. et al. Self-assembly of copper–DNAzyme nanohybrids for dual-catalytic tumor therapy. *Angew. Chemie Int. Ed.* **60**, 14324–14328 (2021).
14. Wang, Y., Liu, E., Lam, C. H. & Perrin, D. M. A densely modified M^{2+}-independent DNAzyme that cleaves RNA efficiently with multiple catalytic turnover. *Chem. Sci.* **9**, 1813–1821 (2018).
15. Nowakowski, J., Shim, P. J., Prasad, G. S., Stout, C. D. & Joyce, G. F. Crystal structure of an 82-nucleotide RNA-DNA complex formed by the 10-23 DNA enzyme. *Nat. Struct. Biol.* **6**, 151–156 (1999).
16. Zaborowska, Z., Fürste, J. P., Erdmann, V. A. & Kurreck, J. Sequence requirements in the catalytic core of the "10–23" DNA enzyme. *J. Biol. Chem.* **277**, 40617–40622 (2002).
17. Vögeli, B., Olsson, S., Güntert, P. & Riek, R. The exact NOE as an alternative in ensemble structure determination. *Biophys. J.* **110**, 113–126 (2016).
18. Elstner, M., Hobza, P., Frauenheim, T., Suhai, S. & Kaxiras, E. Hydrogen bonding and stacking interactions of nucleic acid base pairs: a density-functional-theory based treatment. *J. Chem. Phys.* **114**, 5149–5155 (2001).
19. Kisseleva, N., Khvorova, A., Westhof, E. & Schiemann, O. Binding of manganese(II) to a tertiary stabilized hammerhead ribozyme as studied by electron paramagnetic resonance spectroscopy. *RNA* **11**, 1–6 (2005).
20. Rosenbach, H. et al. Influence of monovalent metal ions on metal binding and catalytic activity of the 10–23 DNAzyme. *Biol. Chem.* **402**, 99–111 (2020).
21. Balbach, J. et al. Protein folding monitored at individual residues during a two-dimensional NMR experiment. *Science* **274**, 1161–1163 (1996).
22. Etzkorn, M., Böckmann, A. & Baldus, M. Kinetic analysis of protein aggregation monitored by real-time 2D solid-state NMR spectroscopy. *J. Biomol. NMR* **49**, 121–129 (2011).
23. Nawrot, B. et al. Mapping of the functional phosphate groups in the catalytic core of deoxyribozyme 10-23. *FEBS J.* **274**, 1062–1072 (2007).

Methods

DNA and RNA constructs

A list of all nucleotide sequences and modifications used in this study is provided in Extended Data Fig. 1a.

FRET-based activity assays

For FRET-based activity assays of the Dz variants, an RNA substrate labelled with a fluorescein molecule at the 5′ end and a black hole quencher (BHQ-1) at the 3′ end was used (Biomers.net GmbH). The assay was carried out with 0.1 μM pre-formed RNA–Dz complex at 37 °C in buffer containing 50 mM Tris-HCl pH 7.5, 0.1 mM EDTA and 100 mM NaCl as well as the different concentrations of $MgCl_2$ or $MnCl_2$. Control experiments were performed in the absence of Dz as well as in the absence of Mg^{2+} or Mn^{2+}. To facilitate complex formation, 0.8 μM of RNA substrate and DNAzyme were denatured in buffer in the absence of Mg^{2+} or Mn^{2+} at 73 °C for 5 min and cooled down to room temperature for 15 min. The resulting pre-formed complexes were diluted 1:4 with buffer, and 20 μl of the solution was pipetted into the wells of a 384-well non-binding microplate (Greiner Bio-One). The plate was sealed with tape (Polyolefine Acrylate, Thermo Scientific), placed inside the plate reader (CLARIOStar, BMG LABTECH) and equilibrated to 37 °C for 30 min. Afterward, the seal was removed and the reaction was started by injection of 10 μl (buffered) $MgCl_2$/$MnCl_2$ freshly prepared stock solutions leading to the final concentrations of divalent metal ions of the respective conditions. In cases where different volumes of stock solutions were injected, compensating buffer volumes were previously added to the respective wells. Data points were obtained every 5, 3 or 2 s, depending on the $MgCl_2$ or $MnCl_2$ concentration and therefore on the speed of the reaction. For conditions that induce a large deviation in FRET signal, initial data points detected directly after injection were omitted where applicable to avoid larger error margins originating from initial mixing effects. A coupled automated injection-detection system allowed to compensate the starting-time shifts between different wells. Excitation and emission wavelengths were 484 nm and 530 nm, respectively. We have previously shown that the detected fluorescence emission intensity obtained from this assay correlates well with the fraction of Dz-cleaved RNA substrate[20].

For FRET-based mutation screens, the Mn^{2+}-induced cleavage of the respective variants was determined in reference to the 5C variant, which showed full cleavage under the applied conditions (validated by denaturing PAGE). Each condition was tested in triplicates following the protocol described above with manual addition of Mn^{2+} to a final concentration of 0.4 mM and a subsequent read-out time of 3 h using a Tecan Spark instrument. Clear measurement outliers in triplicates related to air bubbles or RNase contamination (occurring only in less than 3% of the data) were excluded from data analysis. Shown error margins represent the standard deviation of respective triplicates.

Activity assay with fluorescein-labelled RNA substrates followed by denaturing PAGE

Gel-based activity assays were performed with 0.4 μM 5′-fluorescein-labelled RNA substrate (biomers.net GmbH) and 0.4 μM Dz in a total volume of 10 μl 50 mM Tris-HCl pH 7.5 with 0.1 mM EDTA and 100 mM NaCl in the presence and absence of Mg^{2+}, Mn^{2+}, $[Co(NH_3)_6]^{3+}$ or Co^{2+}. Initial Dz–RNA complexes were prepared by incubating the solution containing all components (without Mg^{2+}, Mn^{2+}, $[Co(NH_3)_6]^{3+}$ or Co^{2+}) at 73 °C for 5 min and cooling down to room temperature for 15 min. The reaction was started by adding $MgCl_2$, $[Co(NH_3)_6]^{3+}$, $MnCl_2$ or $CoCl_2$ to the indicated final concentrations. Unless stated otherwise, incubation time was 3 h at 37 °C. The reaction was stopped in 95% ice-cold formamide with 25 mM EDTA followed by boiling the sample for 5 min at 95 °C. Separation of the samples was carried out on 18% polyacrylamide gels with 7 M urea buffered with Tris-borate EDTA buffer (TBE; that is, 89 mM Tris, 89 mM boric acid and 2 mM EDTA, pH 8.0) for 1 h at 20 W. Visualization of fluorescein-labelled RNA substrates was carried out by fluorescence detection. Images were acquired using the ChemiDoc MP System (Bio-Rad).

Denaturing PAGE with unlabelled RNA

Assays with the 2′F-substituted RNA substrate were performed with 10 μM of the RNA substrate and 10 μM DNAzyme in a total volume of 10 μl in 50 mM Tris-HCl pH 7.5 and 100 mM NaCl. RNA and DNAzyme were denatured in buffer in the absence of Mg^{2+} at 73 °C for 5 min, followed by incubation for 15 min at room temperature. Subsequently, Mg^{2+} was added to a final concentration of 10 mM. The mixture was incubated at 37 °C for 3 h. Separation of the samples was carried out on 18% polyacrylamide gels with 7 M urea buffered TBE for 1 h at 20 W. For visualization, the gel was incubated in TBE buffer containing a 1:10,000 dilution of GelRed (Biotium) for 1 h. Images were acquired using the ChemiDoc MP System (Bio-Rad).

EPR measurements

The EPR signal of free Mn^{2+} in an aqueous solution ($Mn(H_2O)_6^{2+}$) consists of six lines. Binding of Mn^{2+} to a DNAzyme–RNA complex induces a ligand field asymmetry and an increase of the rotational correlation time, which leads to such a strong line broadening that the EPR signal of bound Mn^{2+} cannot be detected at room temperature[19,24,25]. Thus, a comparison of the EPR signal intensity in the absence and presence of the Dz–RNA complex enables the quantification of free and bound Mn^{2+} as well as the number and possibly cooperative nature of the occurring binding sites. The titrations were carried out in a flat cell with samples containing 40 μM of the DNAzyme–RNA complex in 50 mM Tris buffer with 100 mM NaCl and 10% D_2O. For each data point, 2 μl of Mn^{2+} stock solution was added to the 500 μl of the initial sample.

The cw EPR spectroscopic measurements were recorded at X-Band frequency on a Bruker EMX micro-spectrometer equipped with an ER 4103TM resonator (Bruker BioSpin). The spectra were measured at room temperature with a modulation frequency of 100 kHz, modulation amplitude of 5.0 G, microwave frequency of 9.79 GHz, and 1,440 points in the field interval of 2,890–4,090 G. The resulting Mn^{2+} EPR signals were baseline corrected with a polynomial function of third order and doubly integrated (*DI*). The *DI* of each measurement was corrected (DI_{cor}) taking the individual Q-values (*Q*) and microwave powers (*P*) into account ($DI_{cor} = DI / (Q P^{½})$).

Binding isotherms were constructed by plotting the concentration of bound Mn^{2+} divided by the concentration of the Dz^{5C}–RNA^{2F} complexes versus the concentration of the free Mn^{2+}. The concentration of bound Mn^{2+} was determined by comparison of the EPR double integral of the sample containing the Dz^{5C}–RNA^{2F} complex with the EPR double integral of a reference sample at the same total concentration of Mn^{2+}. The reference samples of Mn^{2+} free in solution were measured on each day of data collection freshly prepared from a stock solution ($MnCl_2$, 1 M, Sigma Aldrich).

The EPR binding isotherms were fitted with a non-cooperative and two cooperative models as detailed in the Supplementary Discussion[26].

NMR data acquisition, processing and analysis

Oligomers with NMR-grade purity were ordered from BioSpring and isotope-enriched oligomers from Silantes. Oligomers were resuspended in ultra-pure water and mixed in 1:1 molar ratio for complex formation. Oligomer solutions were then mixed with the same volume of twofold measurement buffer to a final concentration of 50 mM tris(hydroxymethyl-d3)amino-d2-methane (Tris-d11, Merck)/HCl pH 7.5, 10% (v/v) D_2O in the absence or presence of metal ions. For measurements of single-stranded Dz^{5C} and RNA, 50 mM Na_2HPO_4/NaH_2PO_4 pH 7.5, 100 mM NaCl, 10% (v/v) D_2O with or without 10 mM $MgCl_2$ were used. Samples were heated to 72 °C for 5 min and slowly cooled down to room temperature to promote uniform complex formation. NMR data were acquired with 200 μl sample volume in 3-mm tubes

at 37 °C (if not stated otherwise). 4,4-Dimethyl-4-silapentanesulfonic acid (DSS) in the respective buffer was used as an external reference for the chemical shift. Experiments were performed at Bruker Avance III HD$^+$ or NEO spectrometer operating at either 600, 700, 750, 900, 1,100 or 1,200 MHz ^{1}H frequencies using H/N/C triple-resonance, H/N/C/P or H/N/C/F quadruple-resonance cryogenic probes. TOCSY experiments were recorded with 80-ms mixing times and NOESY experiments with 300-ms mixing times, if not used for NOE buildup determination. NMR data were processed using Topspin 4.0.6 (Bruker) or NMRpipe[27], and spectra were analysed and plotted with Topspin 4.0.6, Cara 1.9.1.5[28], or Sparky 3.114[29]. Extracted data were analysed, fitted and plotted with OriginPro 9.0G (OriginLab) or Matlab R2019a (MathWorks) and Python-based scripts. PyMol (2.3.4) was used to analyse the 3D structures and create the figures.

NMR resonance assignment

High-resolution spectra of the Dz states and variants as well as RNA$^{2'F}$ and DNA^c–RNA$^{2'F}$ were recorded using sample concentrations between 100 and 750 µM. Most comprehensive chemical shift assignments were carried out for Dz^{5C}–RNA$^{2'F}$ in 50 mM Tris/HCl pH 7.5, 100 mM NaCl, 1 mM $MgCl_2$, and 10% D_2O at 37 °C. Sequential assignment of DNA was performed by finding matching NOESY cross peaks between base protons H6 or H8 and protons H1′, H2′, H2″ and H3′ of the own and the 5′ adjacent sugar moiety (Extended Data Fig. 2a, b). TOCSY cross peaks between H1′and H2′, H2″, or H1′were used to distinguish between different spin systems. NOE contacts between H6 or H8 of adjacent nucleotides were also used for sequential assignment. Cross peaks between H6 and H5, or H7*, were used to map spin systems to pyrimidines C/U or T in the nucleic acid sequence. RNA peaks were assigned after Dz assignment due to the highly reduced set of unassigned cross peaks in the chemical shift region of H6/H8, H1′and H3′. Since peaks are highly overlapping for H4′, H5′, H5″ and ribonucleic H2′, only a limited number of them could be assigned. Owing to their reduced signal-to-noise ratio at the relevant conditions (pH and temperature) only a few amino and imino peaks could be assigned. Adenosine H2 could only be assigned with a preliminary knowledge of the structure and after full assignment of H6 and H8. H2′and H2″ as well as H5′and H5″ could be distinguished via their different NOE buildup rates towards H1′of the same nucleotide. Carbon nuclei were assigned using 2D [^{1}H,^{13}C]-HSQC-TOCSY and 3D [^{1}H,^{13}C]-HSQC-NOESY experiments with 500 µM ^{15}N,^{13}C-Dz^{5C}–RNA$^{2'F}$. Only deoxyribonucleic C1′could be fully assigned (Extended Data Fig. 2c). Note that ^{31}P-NMR experiments were recorded but did not yield usable information due to limited spectral resolution and sensitivity.

NMR titration experiments

For NMR titration experiments, 2 µl aliquots of stock solutions were subsequently added into an NMR tube containing 200 µl sample. Repetition of identical conditions confirmed that this method gives reproducible data. Mg^{2+} titration was performed using 200 µM Dz^{5C}–RNA$^{2'F}$ complex in 50 mM Tis/HCl buffer pH 7.5, 100 mM NaCl, and 10% (v/v) D_2O and aliquots of $MgCl_2$ stock solution with concentrations of 25.25, 25.5, 51.5, 104, 315, 530, 1.070 and 3.240 mM were added. For Dz^{5C}–RNA$^{2'F}$, the titration was also repeated in the absence of NaCl. The chemical shift and intensity of separated NOESY and TOCSY peaks were extracted from recorded spectra. K_d values were calculated by fitting chemical shift perturbation (CSP) data according to: $CSP = CSP_{max}[Mg^{2+}]/(K_d + [Mg^{2+}])$.

Additionally, maximum CSP values were extracted from chemical shift differences of spectra of Dz^{5C}–RNA$^{2'F}$ at 0 and 50 mM $MgCl_2$.

Mn^{2+} titration was performed using 200 µM Dz^{5C}–Dz$^{2'F}$ complex in 50 mM Tis/HCl buffer (pH 7.5), 100 mM NaCl, 1 mM $MgCl_2$ and 10% (v/v) D_2O and aliquots of $MnCl_2$ stock solution with concentrations of 50.5, 51, 103, 312 and 525 µM were added. The intensities of all resolved NOESY and TOCSY peaks were used to determine the respective relaxation rates. Average PRE rates were calculated from all resolved cross peaks of the individual proton.

^{19}F-based NMR experiments

^{19}F-derived experiments were performed at 700 MHz basic proton carrier frequency and using a H/C/N/F (QCI-F) cryogenic probe using ^{1}H-decoupling of 2.5 kHz (up to 1 s in 1D spectra) during ^{19}F-detection, and vice versa. To obtain insights into the Dz, the Dz^{6xF} variant was used containing 2′-F modifications at positions dG_{-6}, dG_{-5}, G2, C7, A11 and G14. The two ^{19}F-labels in the binding arm served as a reference for sequential 2′–2′distances. However, no ^{19}F-^{19}F NOE cross peaks could be detected in 2D [^{19}F,^{19}F]-NOESY spectra (data not shown), introducing an upper detection limit of the respective correlations of about 6.5 Å. In line with previously reported 2′-*O*-methyl modifications in Dz^{5A} (ref.[30]), the selected 2′-F modifications in the loop region do not affect catalytic activity (Extended Data Fig. 1g). The sample concentrations were 750 µM Dz^{6xF}–RNA$^{2'F}$ and 500 µM Dz^{5C}–RNA$^{2'F}$. ^{19}F 1D spectra were recorded for Dz^{5C}–RNA$^{2'F}$ and Dz^{6xF}–RNA$^{2'F}$, ^{19}F-detected [^{19}F,^{1}H]-HOESY and ^{1}H-detected [^{1}H,^{19}F]-HOESY experiments were only performed with Dz^{6xF}–RNA$^{2'F}$. In the ^{1}H-detected version fluorine shifts for adjacent nucleotides, dG_{-6} and dG_{-5} could be assigned directly. Fluor-saturated STD experiments of Dz^{5C}–RNA$^{2'F}$ were performed with 3-s saturation time and 250 Hz pulse width at −206.6 ppm ^{19}F frequency. For STD experiments with Dz^{6xF}–RNA$^{2'F}$, 50 and 80 Hz saturation pulse width at ^{19}F frequencies of −198.46, −201.15, 201.635, −202.1 and −202.8 ppm were used. ^{19}F-substituted nucleotides could be assigned by using strong STD peaks of geminal H2′and vicinal H1′peaks displaying splitting due to the J_{FH} coupling, which can also be detected in homonuclear [^{1}H,^{1}H] spectra. Same signals also appear in STD spectra with saturation frequencies close-by, but with decreased intensities. This effect is reduced by using more selective saturation pulses with narrow width such as 50 instead of 80 Hz; however, also weaker STD signals are obtained under more selective pulses. Analysis of the different intensities of the known H1′ and H2′peaks at various saturation frequencies and the two different pulse widths enabled the assignment of the fluorine signals. Long-range STD signals could only be assigned for protons in the less crowded chemical shift regions of 1–3 ppm and 6–8 ppm.

Paramagnetic relaxation enhancement

Three sequences containing a substitution of thymidine by 5-ethynyl-2′-deoxyuridine (EdU) at positions dT_{-8}, dT_8 and dT_{+7} (Dz^{EdU-8}, Dz^{EdU8}, Dz^{EdU+7}) were used (BioSpring). dEdU nucleotides were modified with a 4-azido-2,2,6,6-tetramethylpiperidinyl-1-oxy (TEMPO)-azide(N_3) spin-label via Cu(I) click chemistry (Extended Data Fig. 1f). In brief, a 5-fold excess of TEMPO-N_3 was mixed with 2 mM EdU-modified Dz to 80 µl reaction volume, and 24 µl of freshly prepared catalyst solution (one part 0.1 M CuBr and two parts 0.1 M TBTA, both in DMSO/tert-butanol (3:1)) were added. The solution was mixed vigorously and incubated at 25 °C, 800 rpm for 4 h. For purification, 10 µl 3 M NaOAc was mixed with the sample before adding 1 ml cold ethanol (−20 °C), incubating on ice for 20 min, and centrifuging for 1 h at 4 °C and 12,000*g*. The supernatant was discarded, and the pellet was washed twice with cold 70% (v/v) ethanol. The pellet was air-dried for 15 min and then resuspended in 1 ml water. The sample was dialysed against water over night and then again over the day (24 h) in a 3.5 kDa MWCO Slide-A-Lyzer Minidialysis device (2 ml). The sample was freeze-dried overnight (Speed-Vac) and then resolubilized in water and twofold NMR buffer. Homonuclear TOCSY and NOESY spectra were recorded for 220 µM Dz^{EdU-8}–RNA$^{2'F}$ and 350 µM Dz^{EdU8}–RNA$^{2'F}$, and only a TOCSY spectrum was recorded for 100 µM Dz^{EdU+7}–RNA$^{2'F}$. 2 mM ascorbic acid was added, and the samples were incubated for 1 h at 37 °C to reduce and inactivate the paramagnetic spin label. Spectra of the complexes with the inactivated spin-label were recorded under the same conditions as the spectra before. Peak intensity ratios of all accessible cross peaks were extracted, and intensity ratios of all cross peaks derived from the same proton were averaged. Intensities derived from only one cross peak or with a standard deviation exceeding 80% of the average intensity value were excluded from the structure calculations.

T_1 relaxation and hetNOE

^{13}C T_1-relaxation experiments were conducted with 500 µM uniformly labelled ^{13}C,^{15}N-Dz^{5C}–RNA$^{2'F}$ using constant time (ct) modified versions of the pulse program hsqct1etgpsi3d (Topspin 4.0.6). Note that the applied labelling pattern introduces systematic errors in relaxation rates[31] affecting quantitative read-out parameter, in particular for T_2-relaxations measurements that show a similar behaviour as observed for the T_1 relaxation (data not shown), but still enabling a comparative analysis of the DNA dynamics along the Dz sequence. Delays for inversion recovery were set as 20, 100, 250, 500 and 1,000 ms for T_1 determination. H1′-C1′ cross peak intensities were extracted from each spectrum and fitted with the Bloch equation.

HetNOE spectra were recorded without ct modifications, and data were processed with maximum entropy deconvolution (NMRpipe) using $^1J_{CC}$ of 55 Hz to suppress the homonuclear ^{13}C-^{13}C splitting effects. HetNOE enhancement was derived by calculating the H1′-C1′ cross peak intensity ratios of the spectrum and unsaturated reference.

NMR temperature-dependent experiments

TOCSY spectra of single-stranded Dz^{5C}, Dz^{5C}–RNA$^{2'F}$ and Dz^{5C}–RNA products were recorded at temperatures between 60 and 15 °C with decreasing temperatures. Peaks were assigned at temperatures close to 37 °C, their individual temperature shifts were traced, and peak intensities were extracted. Comparison of the spectra of Dz^{5C}–RNA products before and after a denaturing cycle showed that the procedure is reversible. Pyrimidine cross-peak intensities were normalized to their intensity at 37 °C. To facilitate comparison of melting behaviour of different cross peaks (Extended Data Fig. 3b–d), the linear regime of each profile (25 °C < T < 40 °C) was fitted individually to generate comparable slopes.

NOE buildup and eNOEs

NOE buildup data were recorded with an array of [^{1}H,^{1}H]-NOESY spectra of 500 µM Dz^{5C}–RNA$^{2'F}$ using mixing times of 0.5, 5, 10, 20, 30, 40, 80, 120, 180, 260, 400 and 800 ms. NOE cross-peak intensities extracted by peak integration were fitted using a double-exponential buildup function derived from the Solomon equation:

$$I(t_{mix}) = I_{max}\exp(-\varrho \times \sigma \times t_{mix})(1-\exp(-2 \times \sigma \times t_{mix})$$

where $I(t_{mix})$ is the peak intensity at a given mixing time, I_{max} the theoretical maximal intensity, σ the cross-relaxation rate and ϱ the auto-relaxation rate of the NOE buildup. A precise σ can be derived with the eNORA software[32], which considers relative intensities, individual ϱ, transfer mechanism between upper and lower diagonal peaks, and especially proton–proton spin diffusion effects based on a structural model. A full-matrix approach was used, and libraries of the published eNORA scripts were modified to work with nucleic acids and Xplor-NIH 2.49[33] structure files. Since shorter mixing times lead to unreliable data, only intensities derived from t_{mix} between 40 and 800 ms were analysed.

Real-time NMR experiments

Real-time NMR experiments were carried out with 200 µl pre-equilibrated Dz^{5C}–RNA complexes in the 100 mM NaCl. The reaction was started by the addition of 1 mM $MgCl_2$. The lag time between sample mixing and the start of the acquisition was approximately 2 min. A series of 280 ^{1}H 1D experiments was recorded over a time course of 12 h after the addition of $MgCl_2$. Alternatively, a 2D homonuclear TOCSY spectrum with 3 h duration and 64 increments was started after the addition of 1 mM $MgCl_2$. Several identical experiments were recorded to ensure that an endpoint is reached. In addition to the 3 h experiment, a longer [^{1}H,^{1}H]-TOCSY and a [^{1}H,^{1}H]-NOESY experiment were also recorded 24 h after the reaction was initiated in order to obtain better insights into the product state. Data analysis is described in more detail in the Supplementary Discussion.

Residual dipolar couplings

Residual dipolar coupling (RDC) constants were extracted from [^{1}H,^{13}C]-HSQC spectra recorded with 500 µM ^{15}N,^{13}C-Dz^{5C}–RNA$^{2'F}$ at 20 °C in the presence and absence of 10 mg/ml phage Pf1 (ASLA Biotech) as an alignment medium. For peak assignment at 20 °C, decoupled [^{1}H,^{13}C]-HSQC experiments were acquired. The extracted RDC constants and the structure with the lowest-energy profile from the initial structure calculation were used as input for the Redcat[34] software or the calcTensor tool of Xplor-NIH[33] to calculate a final field tensor of 3.23 magnitude (Da) and a 0.364 rhombicity (R). The calculated field tensor and a 20% reduced set of RDC constants were used as input of the final structure calculation. Theoretical RDC values were calculated using calcTensor from the resulted lowest-energy structure of the ab initio calculation and correlated with the experimental data.

Structure calculation

Conventional NOE restraints were derived from cross-peak integration of a [^{1}H,^{1}H]-NOESY spectrum with 300-ms mixing time. Peak intensities were divided by the average peak intensity of all H6-H5 cross peaks and grouped into weak, intermediate, or strong contacts if the ratio was below 0.1, between 0.1 and 0.5, or higher than 0.5, respectively. Weak contacts were set as distance restraints of 4.1 (2.8–6.7) Å, intermediate contacts as 3.2 (2.0–5.6) Å, and strong contacts as 2.4 (1.2–3.6) Å, where the values in parenthesis represent the lower and upper restraint limits. Restraints derived from heteronuclear fluorine-proton NOE contacts were set as 5.0 (1.0–7.0) Å distance, and as 5.0 (1.0–8.0) Å if derived from STD experiments. Paramagnetic relaxation enhancement ratios of the spin labels were grouped into strong, intermediate, or weak contacts, if ratios were below 0.2, between 0.2 and 0.4, or above 0.4, respectively, and corresponding distance restraints were set to 10.0 (1.0–30.0) Å, 25.0 (10.0–45.0) Å, or 50.0 (25.0–149.0) Å. Note that the used restraining should also take uncertainties in spin-label position into account. Additionally, hydrogen bond distances for Watson–Crick base pairs −9 to −1 and +2 to +9 were restrained according to ref. [35], and restraints for base-pair planarity were used. Structure calculations were performed with the software Xplor-NIH 2.49[33] with 200 runs starting from a randomized initial structure including or excluding RDC restraints. The 20 output structures with the lowest overall energy potential were selected and further analysed to find new long-range NOE restraints. eNOE contacts were calculated from resulting structures, replacing their conventionally derived counterparts. The structure calculation was rerun with the new restraint data, and the process was repeated iteratively until no new long-range NOE and eNOE could be found. Structure refinement was performed using the lowest-energy structure from the ab initio calculation with RDC restraints. For the (otherwise standard) refinement runs, the starting temperature of the simulated annealing stage was reduced from 3,500 K to 350 K.

Angular restraints

In addition to the described distance restraints, dihedral angles were included in the structure calculation. For the A-form helix homology region backbone dihedral angles α, β, γ, δ, ε and ζ were restrained to typical A-form helix values, sugar dihedral angles $\nu_{1\text{-}3}$ to 3′-endo pucker, and χ to *anti* conformation. Additionally, nucleotides were set to *syn* or *anti* conformation according to their relative NOE buildup rates. All angular restraints used for structure calculation are listed in Supplementary Table 2.

Structure refinement

The 100 conformers with the lowest energy were subjected to restrained energy minimization as described in Pimenta et al. (2013)[36] with the AMBER19 software package[37]. The ff99 force field[38] with the "OL3" χ distribution from ff14SB and the parmbsc0 α/γ-modifications, resulting in the Amber ff99OL3 parameters, was used for the RNA. The ff99 force

field[38] with the parmbsc0 α/γ, χ/ζOL1, χOL4 and βOL1 modifications, resulting in the Amber OL15 parameters, was used for the DNA. The structures were protonated with PROPKA[39] according to pH 7.4, neutralized by adding counter ions, and solvated in an octahedral periodic box of TIP3P water molecules[40]. The counter ions were treated with the Joung–Chetham parameters for monovalent ions[41]. The restrained energy minimization was performed in three stages. First, the solute atoms were kept fixed with harmonic positional restraints with a force constant of 500 kcal mol^{-1} $Å^{-2}$ to relax the solvent molecules. Subsequently, the entire system was relaxed after restraint removal. During the last stage, 1,500 steps of NMR-restrained energy minimization were applied with a combination of steepest descent minimization followed by conjugate gradient minimization. A parabolic penalty function with a force constant of 20 kcal mol^{-1} $Å^{-2}$ was used for the NOE upper distance restraints.

The statistics of the NMR-derived structure calculation after refinement are provided in Supplementary Table 1.

Statistics and reproducibility

Reproducibility of the used activity assays was previously confirmed[20]. Key samples for EPR and NMR were tested by preparation with different stocks at different days showing high reproducibility of resulting spectra. Sample stability during NMR measurements was assessed for all conditions via characteristic spectral properties.

MD simulations

After the clustering, the four representative structures were used in all-atom MD simulations involving Mg^{2+} concentrations of 0, 20, 200 and 2000 mM for each structure. Note that the 200 mM Mg^{2+} concentration reflects a similar molar ratio of Mg^{2+}:Dz as present under Mg^{2+} saturation conditions used in the NMR measurements. The structures were surrounded by a shell of TIP3P waters of at least 30 Å thickness, hexahydrated Mg^{2+} ions, counter ions to reach neutrality of the system, and KCl at a concentration of 150 mM; the system was assembled using Packmol-Memgen[42]. The Mg^{2+} ions were placed at least 7 Å away from the Dz–RNA. The same force field parameters were used as in the NMR-restrained minimization step, except that the Mg^{2+} ions were treated with Li–Merz parameters for twofold positively charged metal ions[43]. To cope with long-range interactions, the particle mesh Ewald method[44] was used. The SHAKE algorithm[45] was applied to bonds involving hydrogen atoms, and a direct-space, non-bonded cut-off of 8 Å was used. Initially, 17,500 steps of steepest descent and conjugate gradient minimization were performed; during 2,500, 10,000 and 5,000 steps, positional harmonic restraints with force constants of 25 kcal mol^{-1} $Å^{-2}$, 5 kcal mol^{-1} $Å^{-2}$ and zero, respectively, were applied to the solute atoms. After that, 50 ps of NVT (constant number of particles, volume and temperature) MD simulations were conducted to heat up the system to 100 K, followed by 300 ps of NPT (constant number of particles, pressure and temperature) MD simulations to adjust the density of the simulation box to a pressure of 1 atm and to heat the system to 300 K. During these steps, a harmonic potential with a force constant of 10 kcal mol^{-1} $Å^{-2}$ was applied to the solute atoms. As the final step in thermalization, NVT-MD simulations were performed while gradually reducing the restraint forces on the solute atoms over six steps of 50 ns each from 5 kcal mol^{-1} $Å^{-2}$ to zero. This was done because the structures were investigated in equilibrium with Mg^{2+} in the NMR experiments, but the starting structures of the MD simulations do not have Mg^{2+} bound. The gradual reduction of restraints allows Mg^{2+} to bind to energetically favourable sites at the structures[46] and to compensate high local negative charges of the backbone. Afterward, ten independent production runs of NVT-MD simulations with 1 µs length each were performed. For this, the starting temperatures of the MD simulations at the beginning of the thermalization were varied by a fraction of a Kelvin.

To calculate per-nucleotide Mg^{2+}-binding rates, we used the mindist command from cpptraj[47], measuring the minimal distance for each individual nucleotide to any Mg^{2+} and considered a distance of less than 4 Å to indicate an interaction. Frames in which Mg^{2+} interacted with the residue of interest were divided by the number of total frames for each cluster and the Mg^{2+} concentration.

The box plot shown in Fig. 2c displays all data points (dots). The centre line displays the median and the box limits indicate the upper and lower quartiles, respectively. The dashed line provides reference of starting structure.

The snapshot shown in Fig. 3f was taken from replica 3 of cluster I in the presence of 20 mM Mg^{2+} at time point 820 ns.

Reporting summary

Further information on research design is available in the Nature Research Reporting Summary linked to this paper.

Data availability

NMR resonance assignments of Dz^{5C}–RNA^{2F} are available via the BMRB with the accession code: 34654. Atomic coordinates of the Dz^{5C}–RNA^{2F} ensemble (cluster I) are deposited in the PDB under the accession code: 7PDU. Coordinates of additional cluster and scripts for data analysis are available from the corresponding author upon reasonable request.

Code availability

The codes used for structure calculation, MD simulations and simulation of real-time NMR data are available from the corresponding author upon reasonable request.

24. Horton, T. E., Clardy, D. R. & DeRose, V. J. Electron paramagnetic resonance spectroscopic measurement of Mn^{2+} binding affinities to the hammerhead ribozyme and correlation with cleavage activity. *Biochemistry* **37**, 18094–18101 (1998).
25. Hunsicker-Wang, L., Vogt, M. & Derose, V. J. EPR methods to study specific metal-ion binding sites in RNA. *Methods Enzymol.* **468**, 335–367 (2009).
26. Rinnenthal, J., Klinkert, B., Narberhaus, F. & Schwalbe, H. Modulation of the stability of the *Salmonella* fourU-type RNA thermometer. *Nucleic Acids Res.* **39**, 8258–8270 (2011).
27. Delaglio, F. et al. NMRPipe: a multidimensional spectral processing system based on UNIX pipes. *J. Biomol. NMR* **6**, 277–293 (1995).
28. Keller, R. L. J. *Computer Aided Resonance Assignment Tutorial* (Cantina, 2004).
29. Lee, W., Tonelli, M. & Markley, J. L. NMRFAM-SPARKY: enhanced software for biomolecular NMR spectroscopy. *Bioinformatics* **31**, 1325–1327 (2015).
30. Schubert, S. RNA cleaving '10-23' DNAzymes with enhanced stability and activity. *Nucleic Acids Res.* **31**, 5982–5992 (2003).
31. Thakur, C. S., Luo, Y., Chen, B., Eldho, N. V. & Dayie, T. K. Biomass production of site selective 13C/15N nucleotides using wild type and a transketolase E. coli mutant for labeling RNA for high resolution NMR. *J. Biomol. NMR* **52**, 103–114 (2012).
32. Orts, J., Vögeli, B. & Riek, R. relaxation matrix analysis of spin diffusion for the NMR structure calculation with eNOEs. *J. Chem. Theory Comput.* **8**, 3483–3492 (2012).
33. Schwieters, C. D., Kuszewski, J. J., Tjandra, N. & Marius Clore, G. The Xplor-NIH NMR molecular structure determination package. *J. Magn. Reson.* **160**, 65–73 (2003).
34. Valafar, H. & Prestegard, J. H. REDCAT: a residual dipolar coupling analysis tool. *J. Magn. Reson.* **167**, 228–241 (2004).
35. Huang, K. et al. Solution structure of the MEF2A–DNA complex: structural basis for the modulation of DNA bending and specificity by MADS-box transcription factors. *EMBO J.* **19**, 2615–2628 (2000).
36. Pimenta, J. et al. NMR solution structure and SRP54M predicted interaction of the N-terminal sequence (1-30) of the ovine Doppel protein. *Peptides* **49**, 32–40 (2013).
37. Case, D. A. et al. *Amber 2020* (Univ. California, 2020).
38. Wang, J., Cieplak, P. & Kollman, P. A. How well does a restrained electrostatic potential (RESP) model perform in calculating conformational energies of organic and biological molecules? *J. Comput. Chem.* **21**, 1049–1074 (2000).
39. Bas, D. C., Rogers, D. M. & Jensen, J. H. Very fast prediction and rationalization of pKa values for protein-ligand complexes. *Proteins* **73**, 765–783 (2008).
40. Jorgensen, W. L., Chandrasekhar, J., Madura, J. D., Impey, R. W. & Klein, M. L. Comparison of simple potential functions for simulating liquid water. *J. Chem. Phys.* **79**, 926–935 (1983).
41. Joung, I. S. & Cheatham, T. E. Determination of alkali and halide monovalent ion parameters for use in explicitly solvated biomolecular simulations. *J. Phys. Chem. B* **112**, 9020–9041 (2008).
42. Schott-Verdugo, S. & Gohlke, H. PACKMOL-Memgen: a simple-to-use, generalized workflow for membrane-protein–lipid-bilayer system building. *J. Chem. Inf. Model.* **59**, 2522–2528 (2019).
43. Li, P., Roberts, B. P., Chakravorty, D. K. & Merz, K. M. Rational design of particle mesh Ewald compatible Lennard-Jones parameters for +2 metal cations in explicit solvent. *J. Chem. Theory Comput.* **9**, 2733–2748 (2013).
44. Darden, T., York, D. & Pedersen, L. Particle mesh Ewald: an N ·log(N) method for Ewald sums in large systems. *J. Chem. Phys.* **98**, 10089–10092 (1993).

45. Ryckaert, J.-P., Ciccotti, G. & Berendsen, H. J. C. Numerical integration of the cartesian equations of motion of a system with constraints: molecular dynamics of n-alkanes. *J. Comput. Phys.* **23**, 327–341 (1977).
46. Hanke, C. A. & Gohlke, H. In *Computational Methods for Understanding Riboswitches* Vol. 553 (eds. Chen, S.-J. & Burke-Aguero, D. H. B.) 163–191 (Academic Press, 2015).
47. Roe, D. R. & Cheatham, T. E. PTRAJ and CPPTRAJ: software for processing and analysis of molecular dynamics trajectory data. *J. Chem. Theory Comput.* **9**, 3084–3095 (2013).
48. Richter, C. et al. Determination of sugar conformation in large RNA oligonucleotides from analysis of dipole–dipole cross correlated relaxation by solution NMR spectroscopy. *J. Biomol. NMR* **15**, 241–250 (1999).
49. Steger, G. Thermal denaturation of double-stranded nucleic acids: prediction of temperatures critical for gradient gel electrophoresis and polymerase chain reaction. *Nucleic Acids Res.* **22**, 2760–2768 (1994).
50. Sugimoto, N. et al. Thermodynamic parameters to predict stability of RNA/DNA hybrid duplexes. *Biochemistry* **34**, 11211–11216 (1995).
51. Poland, D. Recursion relation generation of probability profiles for specific-sequence macromolecules with long-range correlations. *Biopolymers* **13**, 1859–1871 (1974).

Acknowledgements We acknowledge access to the Jülich-Düsseldorf Biomolecular NMR Center. We thank H. Arthanari, A. Boeszoermenyi and T. Viennet for valuable support regarding the ^{19}F-NMR experiments; R. Biehl for helpful discussions; and R. Kümmerle for data acquisition at 1.1 GHz. H.G. is grateful for computational support and infrastructure provided by the "Zentrum für Informations-und Medientechnologie" (ZIM) at the Heinrich Heine University Düsseldorf and the John von Neumann Institute for Computing (NIC) (user ID: HKF7, VSK33). This work was supported by the German Research Foundation (DFG) (ET 103/2-1, ET 103/2-2, ET 103/4-1, and ET 103/5-1) to M.E., the Chemical Industry Fund (Li 196/05 to I.S. and Hoe 700080 to H.R.), the German Academic Scholarship Foundation (to H.R.), the Bayer AG (Grants4Ag program to I.S.), and the European Union's Horizon 2020 research and innovation program under the Marie Sklodowska-Curie grant agreement number 660258 to A.V. The Center for Structural Studies is funded by the DFG (grant number 417919780).

Author contributions J.B., J.V., H.R., A.V., C.G.W.G., C.W., M.G., H.K. and M.E. conducted the experiments and/or performed simulations, and, together with G.S., O.S., H.G. and I.S., analysed the data. NMR data acquisition and processing were carried out by J.B., A.V., M.G. and M.E. Activity assays were performed by J.V., H.R., H.K. and M.E. MD simulations were performed by C.G.W.G. EPR spectra were recorded by C.W. J.B., J.V., H.R., D.R., H.G. and M.E. wrote the manuscript. All authors designed the experiments and commented on the manuscript.

Competing interests The authors declare no competing interests.

Additional information

Supplementary information The online version contains supplementary material available at https://doi.org/10.1038/s41586-021-04225-4.

Correspondence and requests for materials should be addressed to Manuel Etzkorn.

Peer review information *Nature* thanks Harald Schwalbe, Scott Silverman and the other, anonymous, reviewer(s) for their contribution to the peer review of this work. Peer reviewer reports are available.

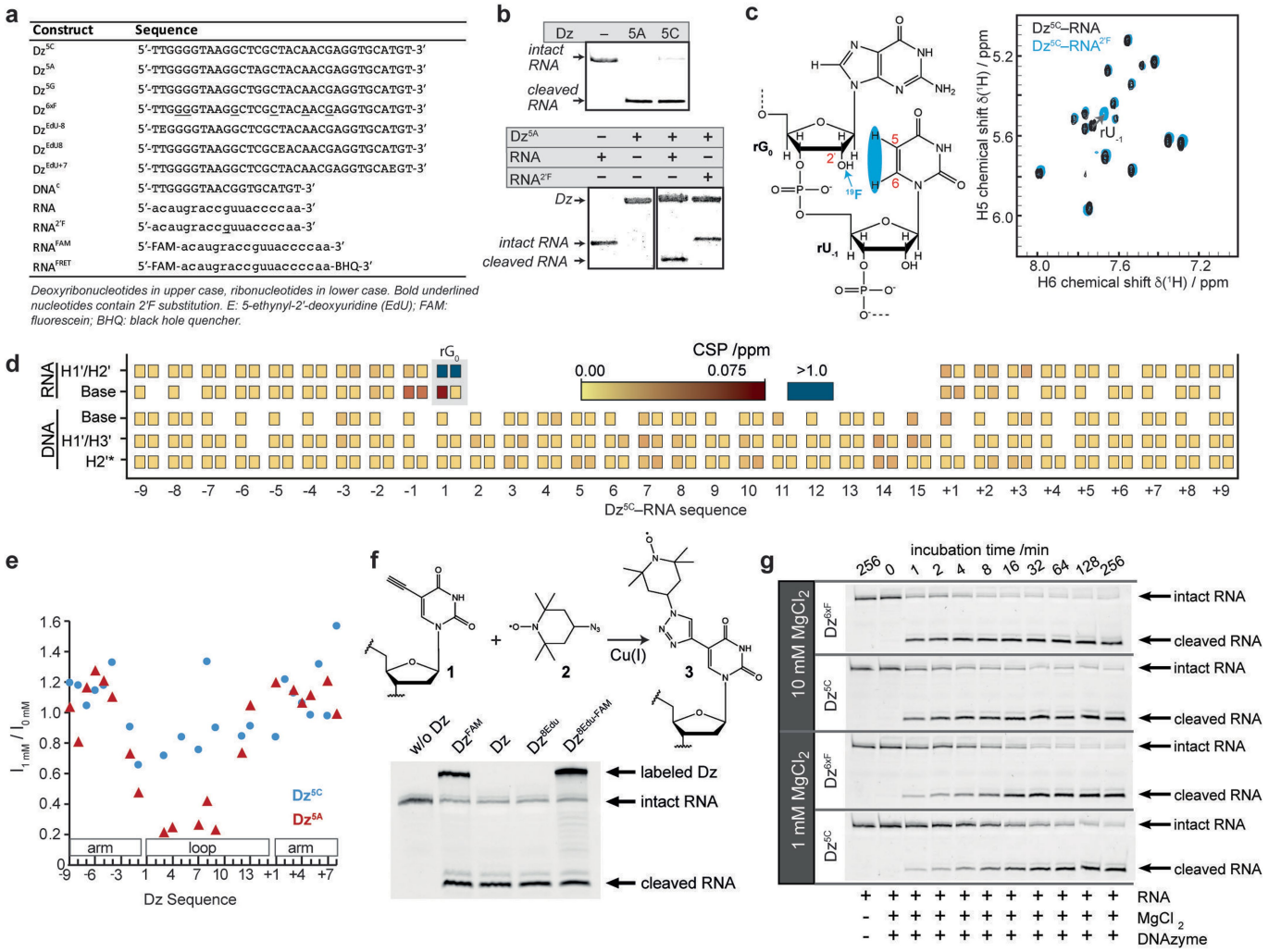

Extended Data Fig. 1 | Properties of used constructs and validation of applied modifications. a) Table of used constructs. b) Gel electrophoretic analysis of substrate cleavage of indicated Dz variants (top, using fluorescein-labelled RNA) and of effects of 2′F stabilization (bottom, using GelRed staining). c) Schematic picture of 2′F RNA modification (left) and affected protons in [^{1}H,^{1}H]-TOCSY fingerprint spectra (Dz^{5C}–$RNA^{2'F}$, blue and Dz^{5C}–RNA, black). The 2′F modification at rG_0 induces CSP only in its direct proximity, i.e., at the H5 and H6 position of rU_{-1}. While the absence of ^{13}C enrichments in the RNA substrate impedes accurate determination of potential effects of the 2′F modification on the pseudorotation phase around the cleavage site[48], analysis of the CSP pattern induced by the 2′F modification at all resolved ^{1}H positions within the complex (d) confirms that the substrate stabilization does not alter the overall structure of the precatalytic complex. e) Nucleotide-specific ratio of peak intensities in the presence and absence of 1 mM Mg^{2+} for Dz^{5A}–$RNA^{2'F}$ (red) and Dz^{5C}–$RNA^{2'F}$ (blue). To enable a reliable comparison between different nucleotides, the changes of the cross-peak intensities of the correlation between H1′ and H6/H8 are shown for each Dz nucleotide. The peak disappearing in the loop region is linked to exchange processes occurring in the NMR intermediate-exchange regime, whereas the otherwise observed CSPs reveal exchange processes in the NMR fast-exchange regime. It can be concluded that Mg^{2+} resides longer within the catalytic loop of the 5A variant, possibly facilitating cleavage. f) Validation of labelling efficiency and cleavage capabilities of the click chemistry approach used for PRE spin labelling. A schematic of the used copper-catalysed click reaction using TEMPO-azide (2) and 5-ethynyl-2′-deoxyuridine (EdU) (1) (f, top). The EdU was used to replace one selected thymine nucleotide in the Dz sequence. To test labelling efficiency and cleavage capabilities, a FAM-azide was used, enabling direct detection via SDS-PAGE (f, bottom). To evaluate the labelling efficiency, identical amounts of a commercial FAM-labelled Dz were loaded on the indicated lane. g) Validation of activity of Dz^{6xF}. Denaturing SDS-PAGE results of time-dependent substrate cleavage of Dz^{5C} without and with the six 2′-^{19}F substitutions (Dz^{6xF}). The data demonstrate that the fluorine atoms do neither affect the Dz's cleavage activity nor Mg^{2+}-dependency.

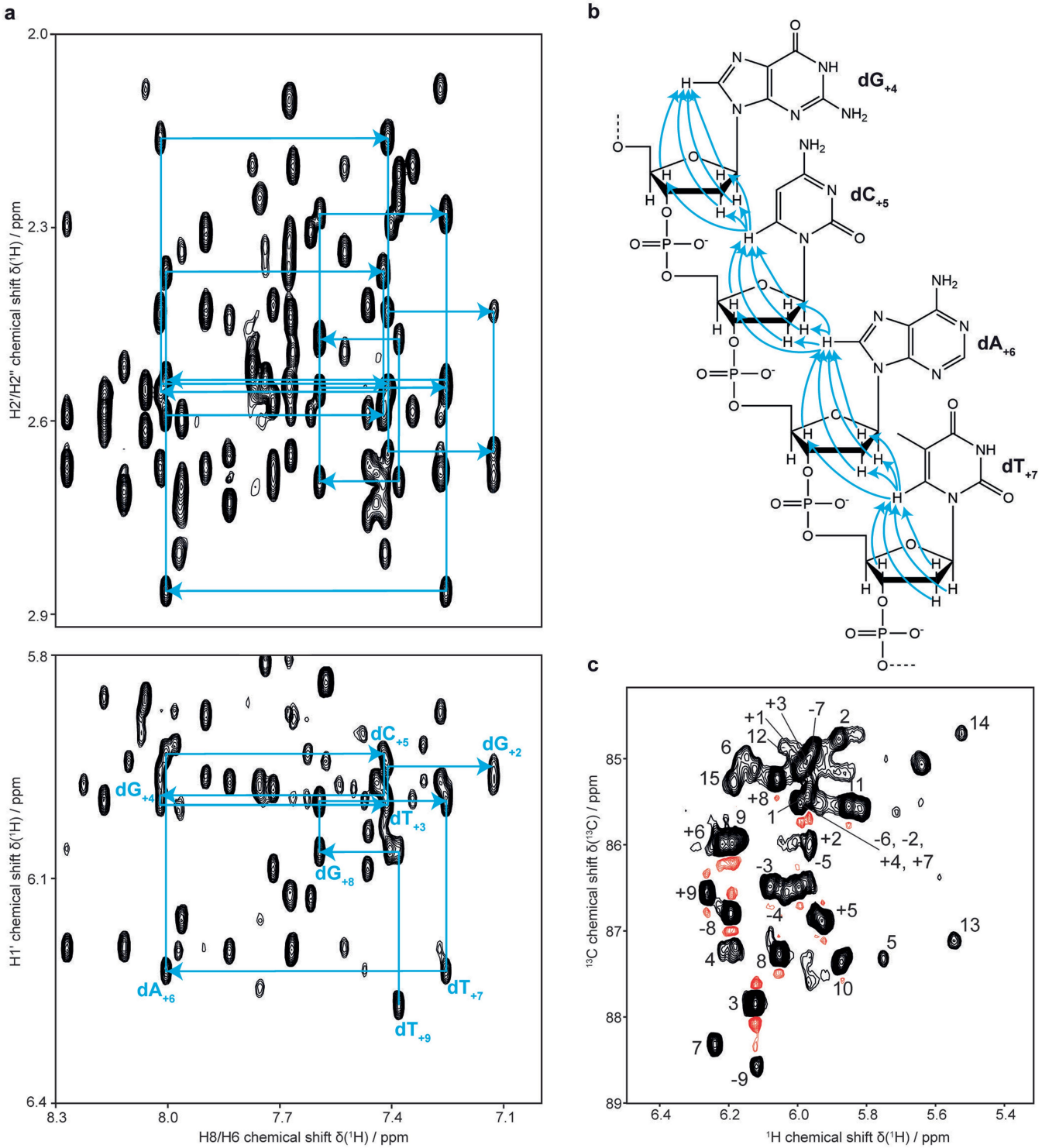

Extended Data Fig. 2 | NMR resonance assignment of Dz^{5C}–RNA$^{2'F}$. a) Extracts of a [^{1}H,^{1}H]-NOESY spectrum showing sequential correlations of the Dz's sequence dG_{+2} to dT_{+9} as indicated in b). c) [^{1}H,^{13}C]-HSQC spectrum showing assignments for 1'-CH groups (see methods for more details).

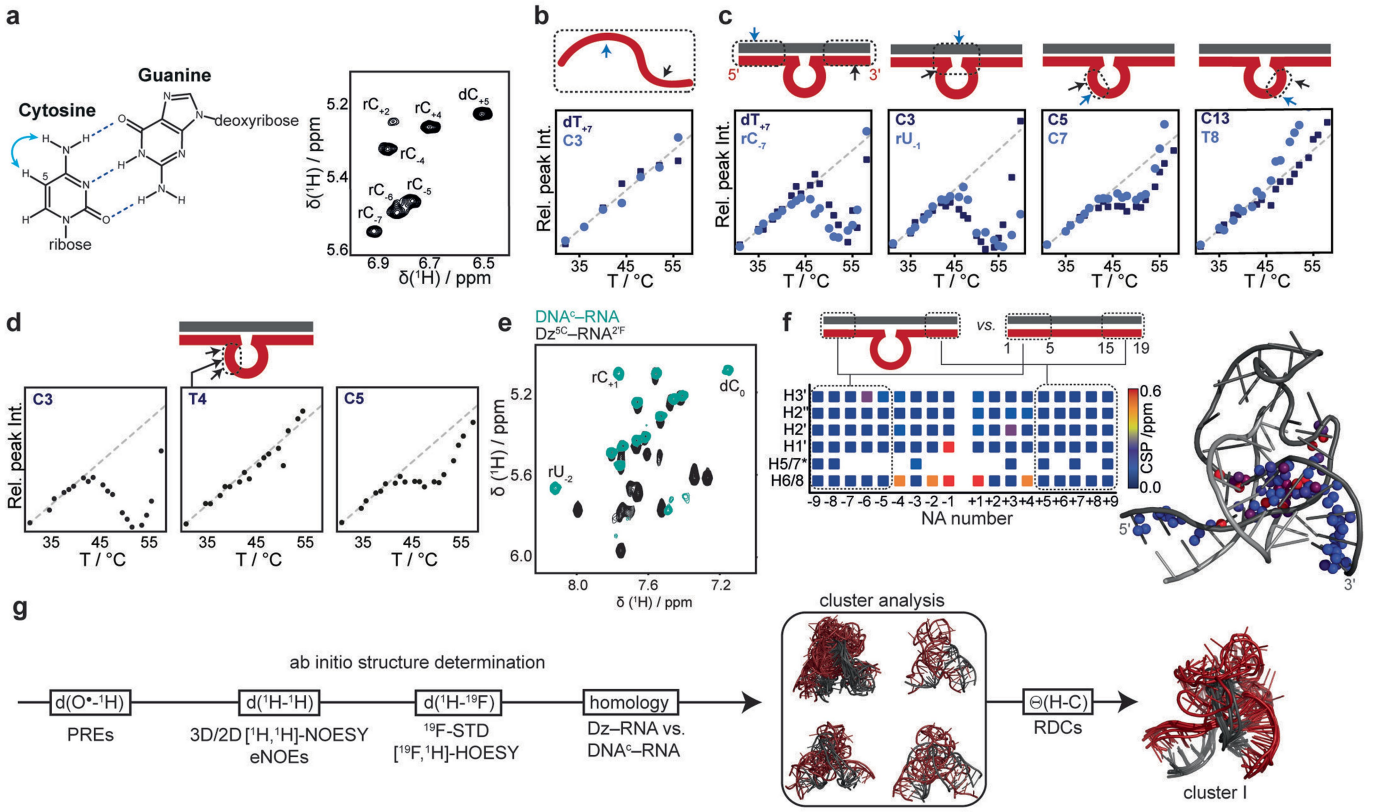

Extended Data Fig. 3 | Molecular properties of the precatalytic state. a) Presence of amino peaks as indicators of stable hydrogen-bond formation (e.g., Watson-Crick base pairing). The spectral extract of a 2D NOESY spectrum (right) containing cross correlations between cytosine H5 and the amino group as schematically highlighted (left). The data show clear signals for all base-paired cytosines present in the binding arms, whereas no signal was detected for any of the five cytosines of the Dz's loop, indicating the absence of stable hydrogen bonding of the respective amino groups. (b,c,d) Temperature-dependent TOCSY NMR peak intensities at increasing temperatures for indicated nucleotides in either single-stranded Dz^{5C} (b) or in the precatalytic Dz^{5C}–$RNA^{2'F}$ complex (c,d). Deviation from a continuous intensity increase indicates denaturing of a locally stabilized structure (see Supplementary Discussion for more details). T4 shows a different behaviour than its neighbours (d). e) Comparison of [¹H,¹H]-TOCSY fingerprint spectra of DNA^{c}·RNA (cyan) and DNA^{5C}·$RNA^{2'F}$ (black). Assignments for most affected nucleotides are indicated and show that in the absence of the catalytic loop, the respective peaks around the cleavage site shift into the region characteristic for a regular duplex structure as found for the rest of the binding arms. f) Distribution of chemical shift perturbations (CSPs) induced by the presence of the catalytic loop. CSPs for all assigned protons of the binding arm region between Dz^{5C}–$RNF^{2'F}$ and DNA^{c}–RNA are shown as contour plot (left) or mapped on the determined structure of the precatalytic complex (right). The latter demonstrates that the regions with strong CSPs agree very well with the regions that differ from the classical A-form helix in the precatalytic complex. g) Schematic representation summarizing the NMR-based structure determination of the precatalytic complex. Indicated distance and homology restraints were combined in an *ab initio* structure calculation, followed by a cluster analysis and conformational filtering using RDCs, resulting in a structural ensemble (cluster I) that best resembles all experimental data (see Methods for details and Extended Data Fig. 4 for representative experimental data).

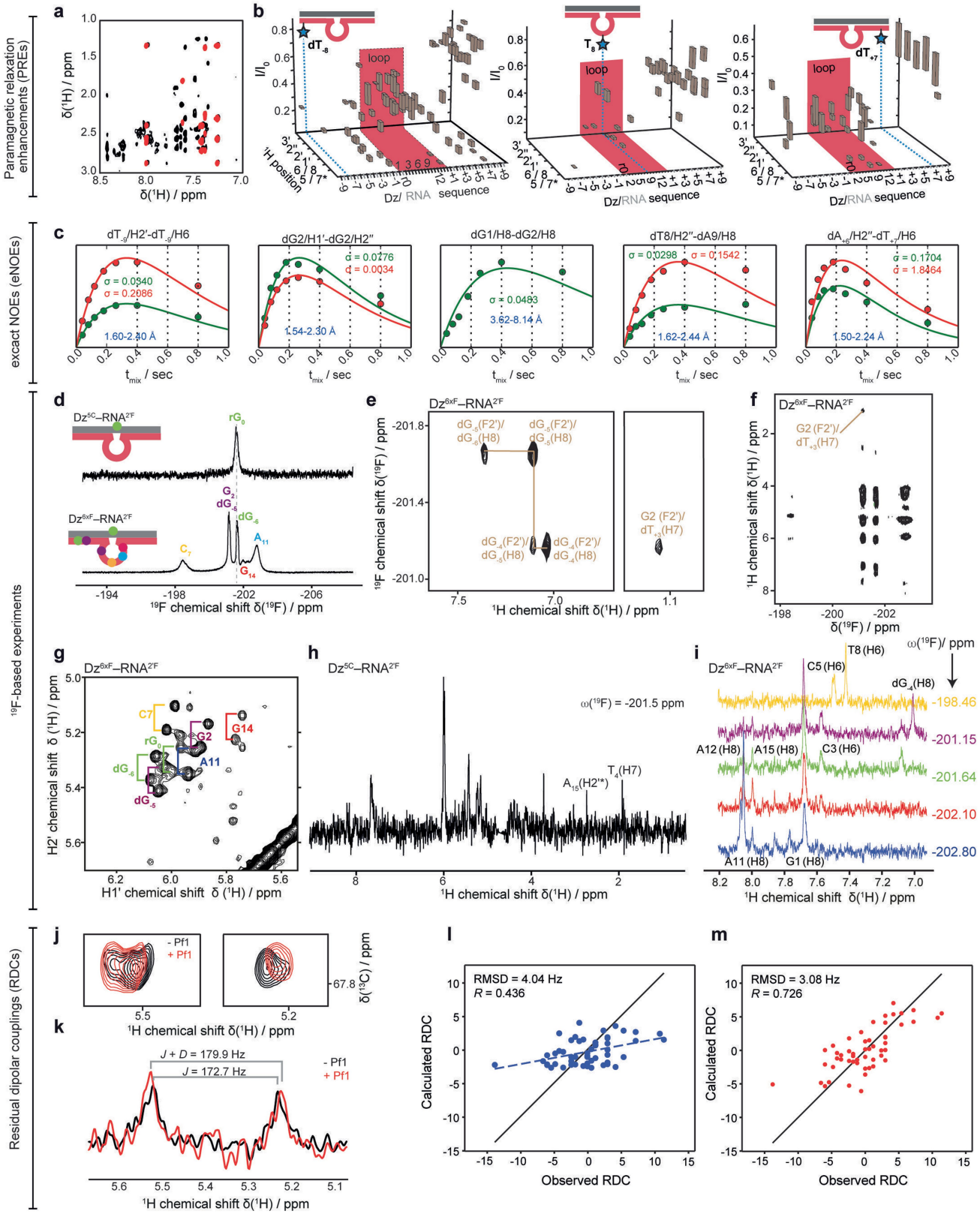

Extended Data Fig. 4 | See next page for caption.

Extended Data Fig. 4 | NMR-based structure determination of Dz^{5C}–$RNA^{2'F}$. a,b) Experimental data and the resulting analysis of the PRE experiments. a) [^{1}H,^{1}H]-NOESY spectral extracts of a sample with a single TEMPO label at position T8 before (red) and after reducing the nitroxide spin label via the addition of ascorbic acid (black). b) The resulting intensity ratios between the two spectra for each resolved proton in the three samples. The marker size (in I/I_0 direction) indicates the error margin (SD) obtained from the analysis of values for all resolved cross peaks of the respective proton. Only protons with at least two different resolved cross peaks were considered. c) Subset of NOE-buildup curves used for the eNOE approach. Normalized NOE intensities recorded with mixing times between 40 and 800 ms (filled circles) and buildup curves (lines) determined by eNORA[32]. [^{1}H,^{1}H]-NOESY cross peaks for the same spin system occurring above (red) or below (green) the diagonal were considered for most NOE contacts. Notably, even short and geometrically fixed distances show considerable differences in their buildup behaviour, demonstrating the necessity to incorporate cross-relaxation effects. Calculated cross-relaxation rates (σ) and extracted eNOE distance range (within 20% error margin) (blue) are indicated. d–i)^{19}F-based NMR experiments. d) 1D ^{19}F-NMR spectra of Dz^{5C}–$RNA^{2'F}$ (top) and of Dz^{5C} variant containing six 2′-^{19}F modifications at position G_{-6}, G_{-5}, G2, C7, A11, and G14 (Dz^{6xF}, bottom) in complex with $RNA^{2'F}$. While [^{19}F,^{19}F]-NOESY spectra of Dz^{6xF}–$RNA^{2'F}$ did not show any detectable peaks (data not shown), ^{1}H-detected (e) or ^{19}F-detected (f) [^{1}H,^{19}F]-HOESY spectra show a limited number of distinct cross correlations that were used for sequential resonance assignments as well as long-range distance restraints. g) H1′ and H2′ protons of the respective fluorinated ribose moieties can be identified in a [^{1}H,^{1}H]-NOESY spectrum via the peak splitting induced by the strong J_{FH} coupling. h+i) To overcome sensitivity limitations of the 2D HOESY correlations, ^{19}F-saturated and ^{1}H-detected STD NMR was used. h) Resulting ^{19}F-STD spectrum of Dz^{5C}–$RNA^{2'F}$. i) ^{19}F-STD spectra of Dz^{6xF}–$RNA^{2'F}$ using the indicated ^{19}F saturation frequencies (color code refers to assignment in panel d). j-m) Characterization of residual dipolar couplings (RDCs). j) Example of RDC-induced frequency shifts in the precatalytic complex. The section shows the H5-C5 cross peak of loop position C13 in a [^{1}H,^{13}C]-HSQC spectra recorded in the absence (black) and presence (red) of Pf1 phage at 20 °C using ^{13}C isotope-labelled Dz^{5C} in complex with unlabelled $RNA^{2'F}$. k) 1D cross section of the cross peaks shown in j) representing experimental limitations due to linewidths, peak overlap and signal-to-noise effects. l,m) Correlation plot of observed and back-calculated RDC constants for a non-matching structure of cluster III (l) and the improved correlation of the structure in cluster I (m). Although experimental limitations introduce larger error margins in the determined values (as visible by RMSD values), an RDC effect is still apparent (as visible by a considerably increased correlation).

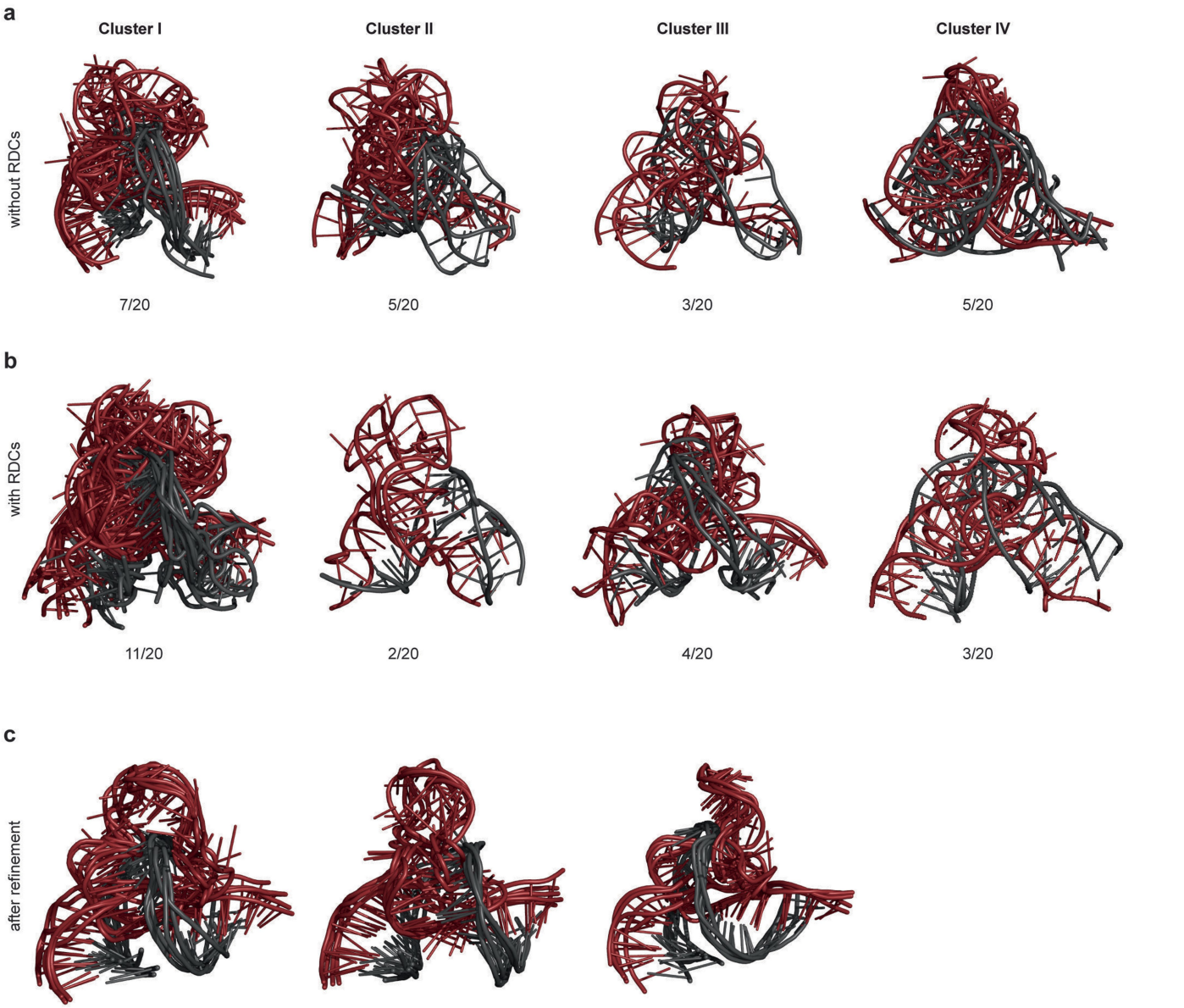

Extended Data Fig. 5 | Characterization of NMR-derived structural ensemble. a) Results of cluster analysis after *ab initio* structure calculation without usage of RDCs. The 20 lowest energy structures (out of 200 calculated) were sorted according to their relative orientation of the Dz loop according to: Full winding around the RNA (cluster I), positioning downstream (cluster II) or upstream (cluster III) of the cleavage site, or other (cluster IV). Numbers below the structures refer to the number of structures in the respective fold. b) Same procedure as in a) but including RDC data. While cluster I is already the most populated in the absence of RDC restraints, it becomes by far the dominant fold after RDCs are included. In general, RDCs can be seen as one of the most reliable NMR-based probes of relative molecular orientation. As such, and albeit the remaining limitation in spectral quality and accuracy (Extended Data Fig. 4j, k), the observed effects on cluster selection appear significant. c) Overlay of the four lowest energy structures (out of 100) for each cluster (cluster I-III) after a more rigorous structural refinement and energy minimization.

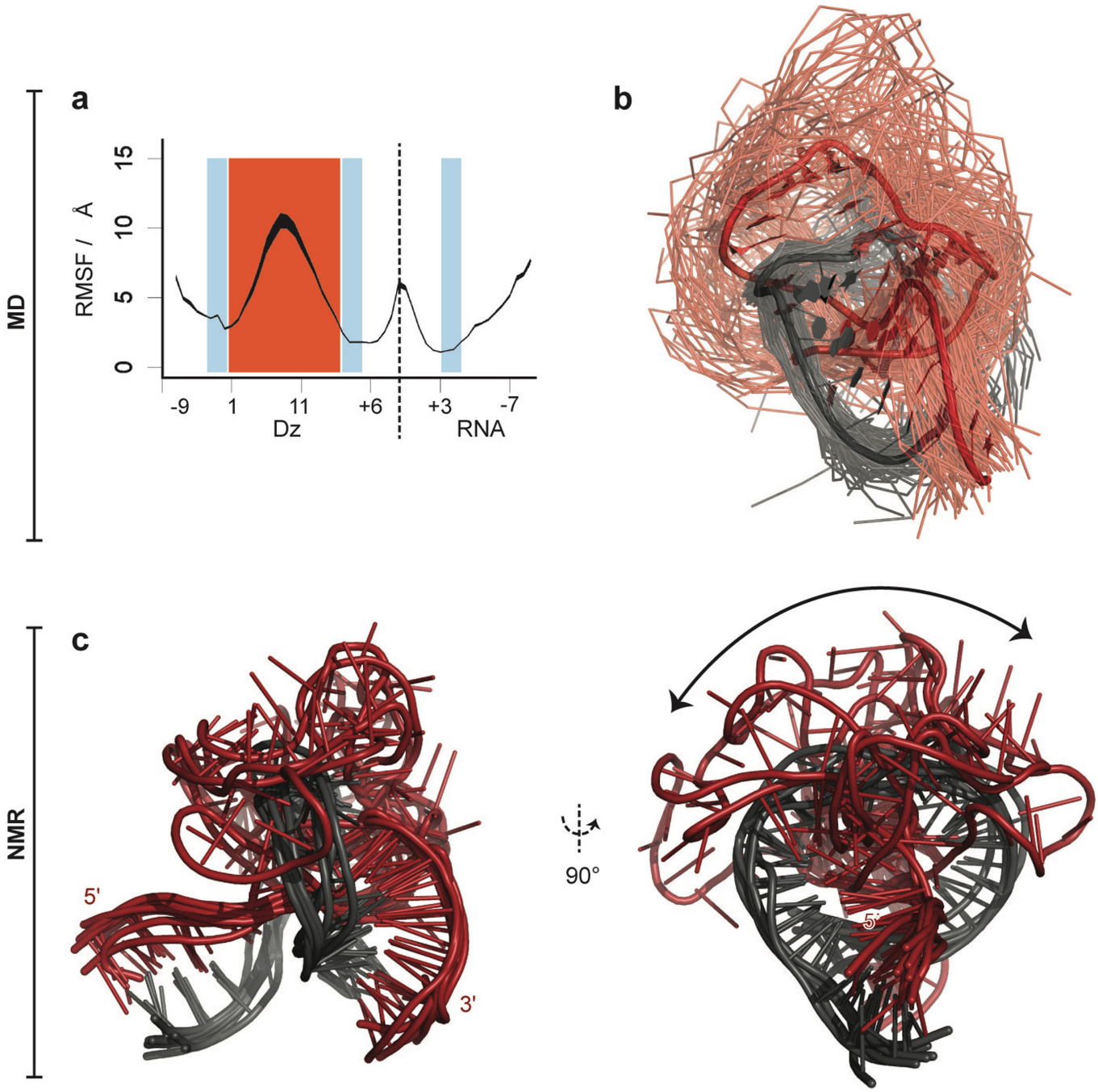

Extended Data Fig. 6 | Conformational plasticity of the precatalytic complex. a) Root mean square fluctuations (RMSF) of Dz^{5C}–RNA during MD simulations. The mean RMSF ± SEM (black area) for each nucleotide over all replicas is shown. The orange area highlights the nucleotides of the catalytic loop, and the blue areas represent nucleotides surrounding the cleavage site. b) Average structure (cartoon) from MD simulations overlaid with the structural ensemble generated from the MD trajectory (semi-transparent ribbon, with structures taken every 10 ns). c) Overlay of all seven lowest energy Dz^{5C}–$RNA^{2'F}$ structures belonging to cluster I and obtained with loose-restraining in the ab initio structure calculation. In contrast to the ensembles shown in Extended Data Fig. 5, here, the loop region was excluded from structure alignment. It can be seen that the core region, including the binding arms and the orientation of the cleavage site, is reasonably well defined with an all-atom RMSD of 2.6 Å. On the contrary, the catalytic-loop region displays pronounced variations in the position within the different structures, providing an estimate of the allowed conformational space. Noteworthy, in direct comparison to the better-defined regions, the loop region does not display largely increased dynamics in the detected time regimes (Fig. 1f) and it still shows stacking interactions of the nucleotides with their neighbours, indicating locally defined conformations (Extended Data Figs. 9d and Supplementary Figure 1). In line with the MD-derived picture, it can hence be assumed that the Dz shows increased conformational plasticity in the loop region compared to the binding arm and, particularly, the cleavage-site region.

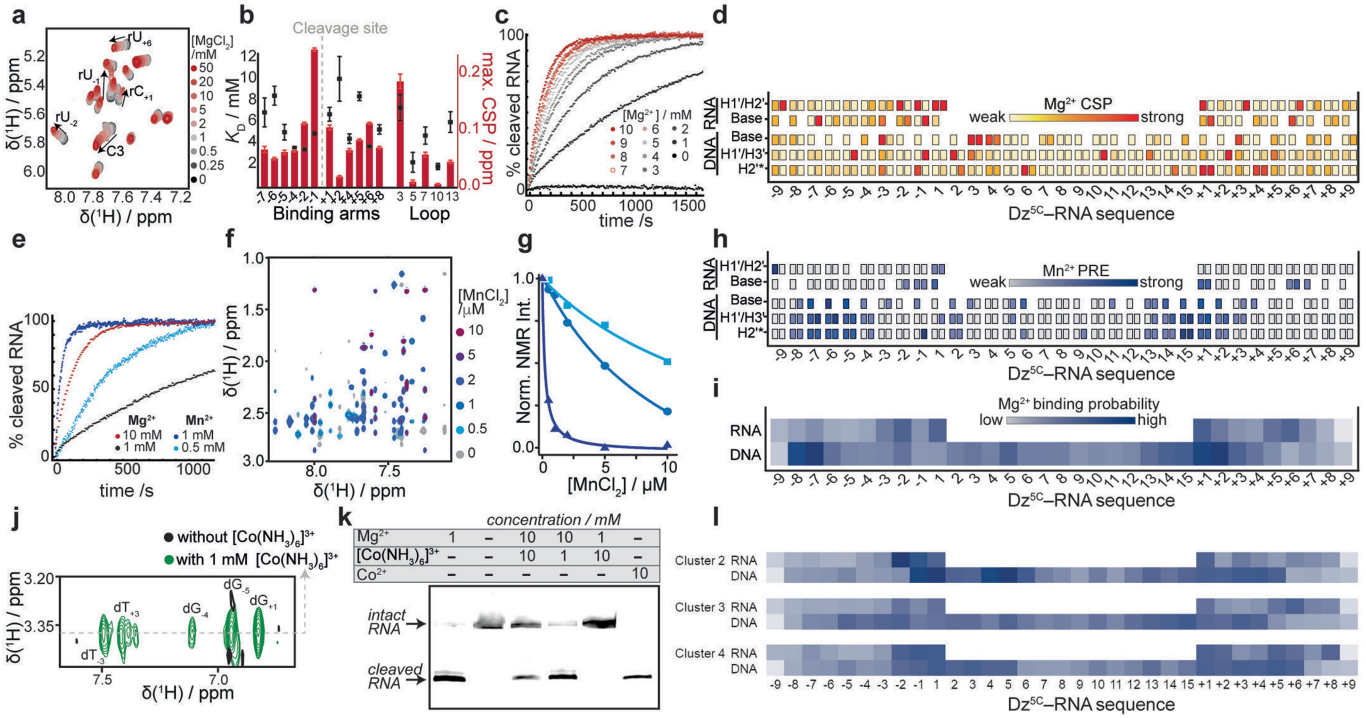

Extended Data Fig. 7 | Metal-ion binding to the precatalytic complex. a) Mg^{2+} binding induces chemical shift perturbations (CSPs) in the fingerprint spectrum of Dz^{5C}–$RNA^{2'F}$ indicative of binding and structural rearrangements occurring in a fast-exchange regime. b) Plot of obtained nucleotide-specific K_D values (black, fitted values ± standard error) as well as the magnitude of Mg^{2+}-induced maximal CSP (red). Note that CSPs report on direct interaction and/or relayed conformational changes. Therefore, the obtained K_D values can only serve as a reporter on effects (either direct or indirect) induced by Mg^{2+} binding. c) Mg^{2+}-dependent cleavage activity as seen by FRET. d) Plot of atom-specific Mg^{2+}-induced CSPs along the Dz–RNA sequence. e) Comparison between Mn^{2+}- and Mg^{2+}-induced activity of Dz^{5C}. f) Mn^{2+} binding in the presence of excess Mg^{2+} does not induce CSPs but clear PRE effects allowing to distinguish between binding and structural changes. g) Different PRE rates for selected nucleotides resulting from differential distances to the Mn^{2+}-binding site. h) Plot of atom-specific Mn^{2+}-induced PRE rates along the Dz–RNA sequence. i) Likelihood of per-nucleotide binding of Mg^{2+} to the precatalytic complex during multiple microsecond-long MD simulations. j) Direct NOE cross peaks between $[Co(NH_3)_6]^{3+}$ and Dz^{5C}–$RNA^{2'F}$. The dashed line indicates the frequency of the hexamine protons. In line with the observed low affinities and fast exchange rates these NOEs point to interactions of the hydration shell of the divalent metal ions with the nucleotides. The observed interactions clearly involve nucleotides of metal-ion binding region I and likely also metal-ion binding region III, confirming that central metal-ion binding sites of the precatalytic Dz–RNA complex adopt a conformation capable of accommodating the hydration shell of divalent metal ions. k) PAGE analysis of Dz^{5C} activity in the presence of indicated concentrations of different metal ions. Interestingly, while Co^{2+} ions can fully activate the Dz and promote substrate cleavage, $[Co(NH_3)_6]^{3+}$ does not mediate the Dz cleavage reaction but does inhibit Mg^{2+}-mediated catalysis. These inhibiting effects are in line with competition for the observed same binding sides. However, the data also suggest that a hydration shell mimic does not maintain a catalytically active state. l) same as i) but, instead of cluster 1 (as used in i), structures of cluster 2–4 were used as starting point of the MD simulations. It can be seen that the MD data using cluster 1 (i) agree considerably better with the experimental data (h) than the other cluster (l), validating the cluster selection based on RDC data.

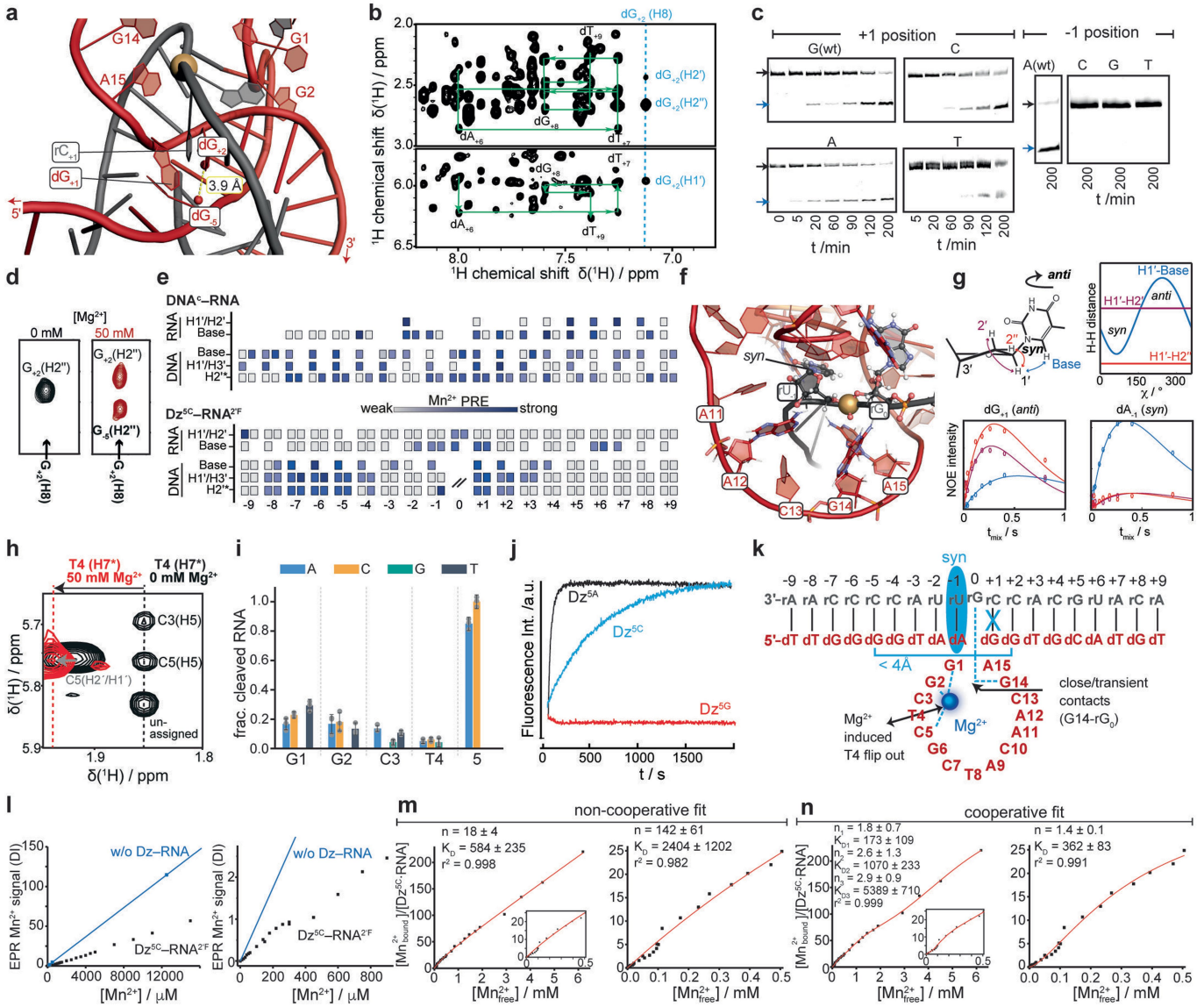

Extended Data Fig. 8 | Experimental links between structure and function of the precatalytic complex. a) The structural features of the scaffolding involve close contacts between the two binding arms, non-base pairing at position +1, and metal-ion binding in region I. b) The clear absence of respective peaks in the NOE pattern confirming flip out of dG_{+1}. Unlike to all nucleotides with expected in-register stacking, no cross correlations of dG_{+1} to dG_{+2} is detected (which should appear along the dashed blue line). Stacking pattern for $dA_{+6} - dT_{+9}$ is shown as positive control (green arrows). c) Effects of mutations at positions +1 and −1 on Dz^{5C} activity confirming that position +1, unlike position −1, does not form an essential Watson-Crick base pair. d) Example of NMR data (extracts of NOESY spectra) confirming close spatial proximity of dG_{-5} and dG_{+2} after Mg^{2+} binding. e) Atom-specific PRE rates obtained from Mn^{2+} titration for DNA^{c}–RNA (top) compared to respective nucleotides in Dz^{5C}–$RNA^{2'F}$ (bottom). The data demonstrate that the presence of the catalytic loop dramatically changes the M^{2+}-binding behaviour of the arms from a rather diffuse pattern (top) to the defined binding region that forms the basis of the scaffolding step (bottom). f) Top view on the precatalytic structure focusing on the cleavage-site surroundings. g) NOE-buildup rates strongly indicate *syn*-conformation of dA_{-1}. The schematic model shown on top visualizes the considered inter-proton interactions with either fixed distances (H1′-H2′, purple, and H1′-H2″, red) or distances strongly depending on the χ-angle (H1′ to indicated base proton, blue). h) NOE pattern indicative of the Mg^{2+}-induced flip out of T4. Note the same behaviour is observed for all ten resolved inter-nucleotide correlations of T4 to its neighbours. i) Changes of cleavage activity by mutations in the 5′ side of the catalytic loop (metal ion-binding site II). Mutations at position 5 serve as a reference; all other mutations are variants of Dz^{5C}. Data are presented as mean values +/- SD of triplicate experiments. j) Comparison of the cleavage activity of the variants Dz^{5A} (black), Dz^{5C} (blue) and Dz^{5G} (red) in the presence of 3 mM Mg^{2+} (data for Dz^{5A} and Dz^{5C} are identical to respective conditions shown in Fig. 1b) . k) Simplified schematic model highlighting the central features of the 3D structure. l-n) cw EPR characterization of Mn^{2+} binding. l) Double integrated EPR signal of Mn^{2+} in the absence (blue) and presence of 40 μM Dz^{5C}·$RNA^{2'F}$ complexes (black). Full range and zoom into lower concentrations are shown. m,n) Fit of experimentally determined binding behaviour (black data points) for either full Mn^{2+} concentration range (left panels) or only the higher affinity binding sites (right panels). Data were fitted to different binding models (red curves, see Methods and Supplementary Discussion for more details on the applied data fitting). n) Three cooperative binding sites were assumed, resulting in high- and low-affinity binding sites and overall the best fit to the obtained data (left). In the right panel, a model with only one cooperative binding site was assumed, and only the shown data range was considered. The shown fit captures the key features of the binding behaviour with minimal number of parameters.

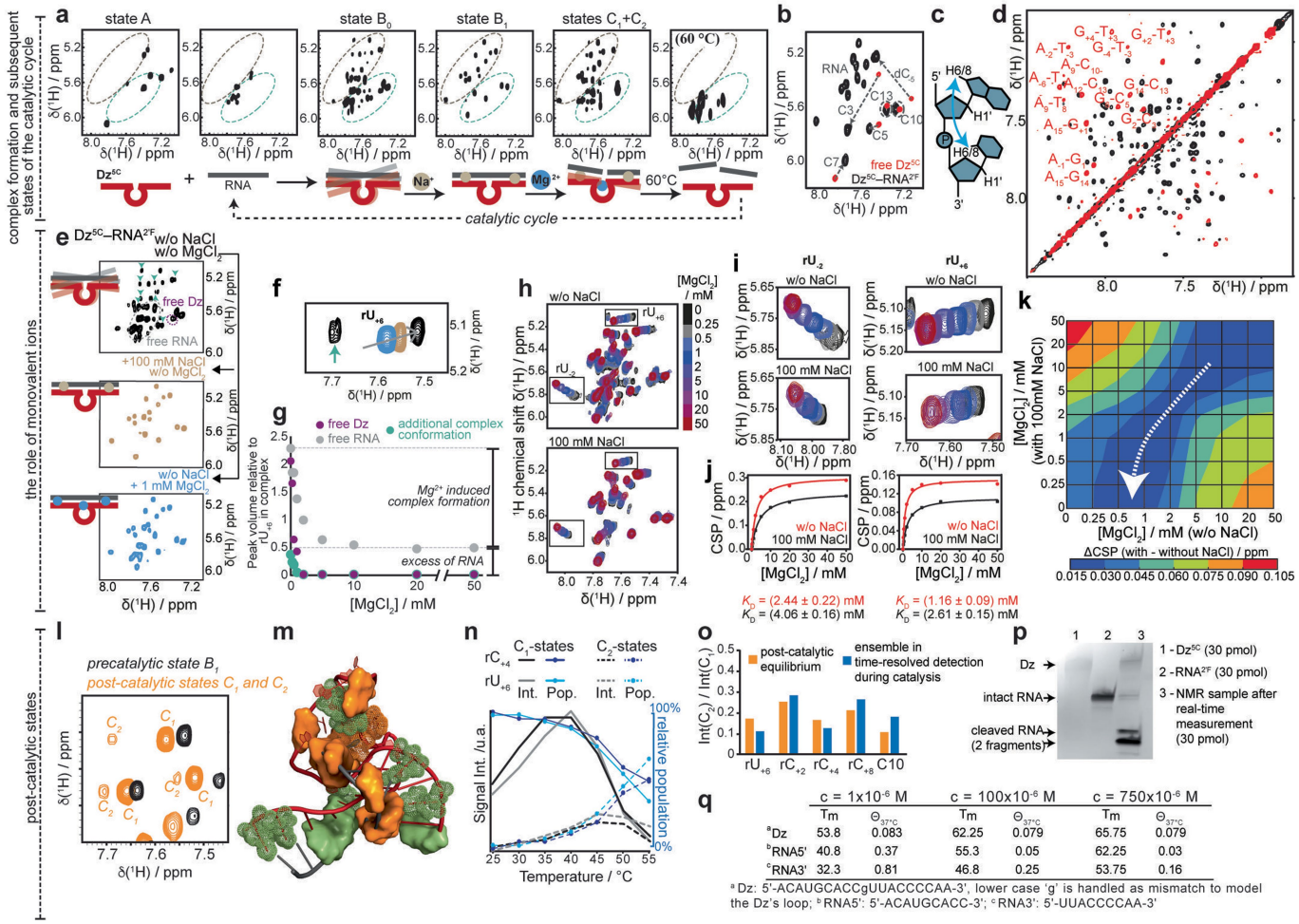

	c = 1x10⁻⁶ M		c = 100x10⁻⁶ M		c = 750x10⁻⁶ M	
	Tm	Θ37°C	Tm	Θ37°C	Tm	Θ37°C
[a]Dz	53.8	0.083	62.25	0.079	65.75	0.079
[b]RNA5'	40.8	0.37	55.3	0.05	62.25	0.03
[c]RNA3'	32.3	0.81	46.8	0.25	53.75	0.16

[a] Dz: 5'-ACAUGCACCgUUACCCCAA-3', lower case 'g' is handled as mismatch to model the Dz's loop; [b] RNA5': 5'-ACAUGCACC-3'; [c] RNA3': 5'-UUACCCCAA-3'

Extended Data Fig. 9 | See next page for caption.

Extended Data Fig. 9 | Properties of central Dz states in the catalytic cycle. a) NMR fingerprint region of indicated states of Dz^{5C} and its substrate in the catalytic cycle. Ellipses as shown in Fig. 1d are overlaid as a reference in each spectrum. The spectra allow to follow complex formation, effects of Na^+ and Mg^{2+}, RNA cleavage and RNA dissociation. Schematic models below spectra illustrate the respective (simplified) conditions and structural features. b) Comparison of the Dz fingerprint region before (red) and after (black) addition of $RNA^{2'F}$. c-d) Analysis of sequential contacts occurring in NOESY spectra of free (red) and complexed Dz (black). c) Schematic of analyzed sequential contacts. d) Extract of spectral region representative of (sequential) cross correlations of the nucleotides' base protons (H6/H8). The data indicate that a central region of the catalytic loop already adopts a (minimally structured) conformation that resembles features found for the same region after complex formation with its substrate (see Supplementary Discussion for more details). e-k) Effects of monovalent (Na^+) metal ions. In the absence of (mono- and divalent) metal ions additional complex conformations are found in the NMR fingerprint spectrum (cyan arrows in e, top). These conformations disappear after addition of either 100 mM Na^+ (e, middle) or 1 mM Mg^{2+} (e, bottom) and do not represent a catalytically relevant state (f, as visible from extrapolation of data from Extended Data Fig. 7a, grey arrow). It is tempting to speculate that this off-pathway state could represent Dz–RNA complexes in an inactive conformation characterized by hybridized binding arms lacking the additional turn of the loop around the substrate. However, other conformations are also possible. In addition to different Dz–RNA complex conformations, the spectrum in the absence of metal ions also shows the occurrence of free RNA and Dz. g) Analysis of peak volumes representative of signal from free RNA (grey), free Dz (purple), and additional complex conformation (cyan). Data were acquired in the absence of NaCl and the presence of indicated concentrations of $MgCl_2$. A rather strong effect on complex formation (population and conformations) is found for the initial (low) Mg^{2+} concentrations. As visible in the spectrum recorded at 100 mM NaCl and absence of $MgCl_2$ (e, middle), both features can also be saturated by NaCl. In other words, under conditions that are more relevant in respect to physiological ionic-strength conditions (e.g. at 100 mM NaCl) complex formation appears to not be a limiting step. However, the data strongly suggest that at low-ionic-strength conditions, strong effects in respect to complex formation and conformation (the latter likely not relevant for catalysis) can be induced by the addition of small amounts of metal ions. This observation may help to clarify previous findings involving a transition from low-ionic strength conditions. h) Results of $MgCl_2$ NMR-titration for fingerprint region of Dz^{5C}–$RNA^{2'F}$ in the absence (top) or presence (bottom) of 100 mM NaCl (the latter is identical to data in Extended Data Fig. 7a). i) Magnification of the behaviour of two indicated nucleotides. While the endpoints of the titrations are very similar in the absence and presence of 100 mM NaCl, the absence of NaCl leads to an extended trend with increased maximal CSPs (j). A roughly 2-fold increased K_D values for Mg^{2+} binding is observed in the presence of NaCl. k) Correlation of the total CSPs (sum of all resolved CSPs) of the respective titration steps in the absence and presence of 100 mM NaCl. For $MgCl_2$ concentration above 1 mM, the presence of NaCl does not have a strong effect on the Mg^{2+}-induced CSPs. By contrast, below 1 mM $MgCl_2$, the minimum of the correlation plot deviates from the diagonal (white arrow). The data indicate that 100 mM NaCl has a comparable effect on the Dz^{5C}–$RNA^{2'F}$ complex structure as approx. 0.7 mM $MgCl_2$. l) Comparison of 2D [^{1}H-^{1}H] TOCSY spectral extracts recorded before (black) and after full cleavage (orange). m) The nucleotides with (orange) or without (green) detected multiple conformations after cleavage highlighted on the structure of the precatalytic complex (dotted representation marks nucleotides with residual uncertainties). n) Detected signal intensities and resulting relative populations of the different states occurring in the post-catalytic complex for indicated nucleotides with increasing temperatures. o) Ratio of NMR peak intensities of the two states for best-resolved nucleotides. The values were calculated after cleavage (orange, data from spectrum in l) as well as from the real-time NMR data during the cleavage reaction (blue, data from spectrum in Extended Data Fig. 10d). The data reveal that the relative population of the respective states is stable over time, including their initial appearance during the cleavage reaction. The observed behaviour can be best explained by a stable equilibrium of slowly exchanging states (see Supplementary Discussion for more details). p) Native PAGE demonstrating cleavage of RNA substrate under NMR conditions (here, the sample after the real-time NMR experiments is shown). q) Theoretical degree of denaturation Θ at 37 °C and denaturation temperatures T_m of Dz complexes with cleaved RNA (calculated with program POLAND[49] using RNA:DNA hybrid parameters[50], loop parameters with *𝜎* = 1*𝑒* − 3[51], dissociation constant *𝛽* = 1*𝑒* − 3, and the given complex concentrations.

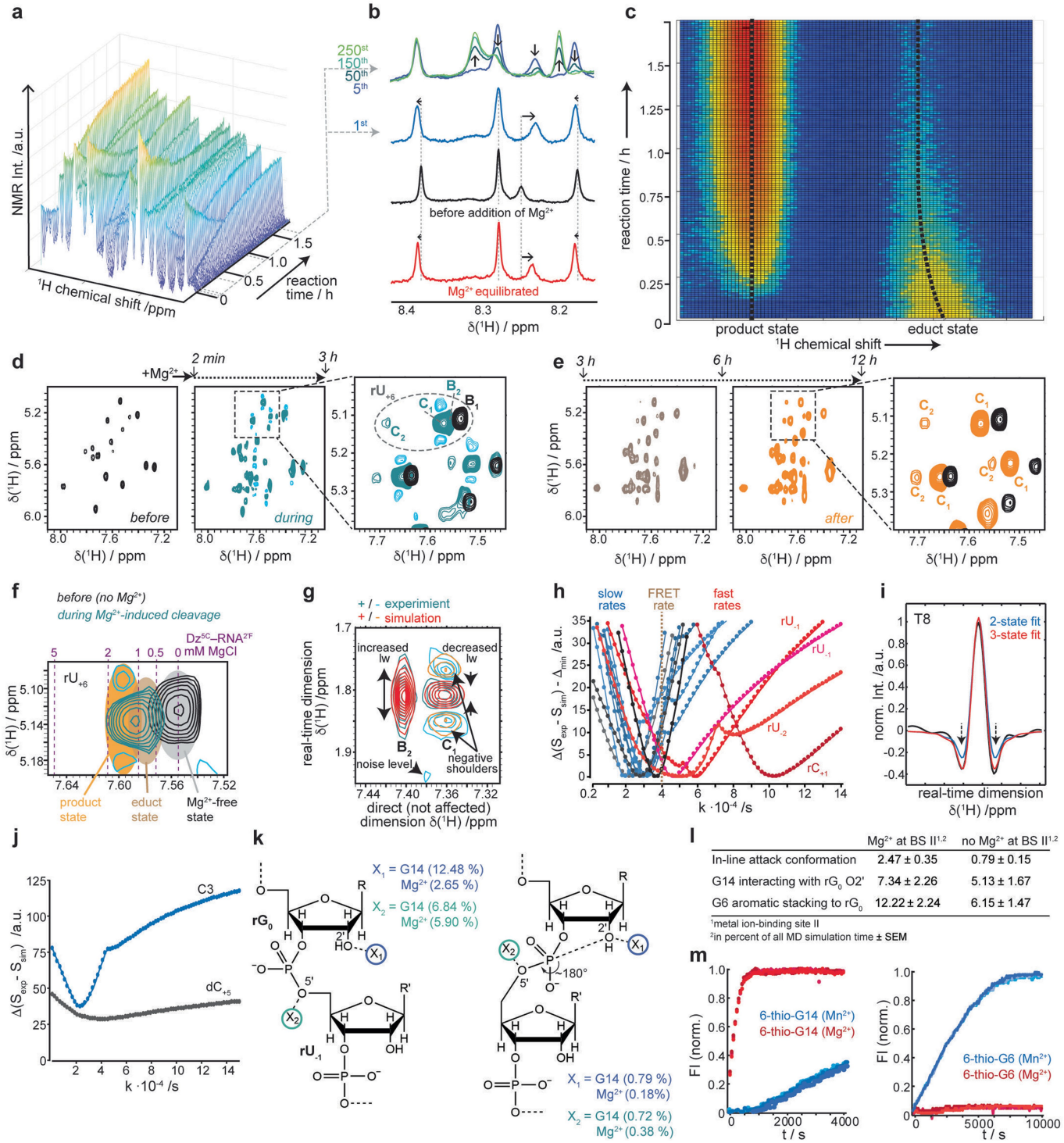

	Mg²⁺ at BS II[1,2]	no Mg²⁺ at BS II[1,2]
In-line attack conformation	2.47 ± 0.35	0.79 ± 0.15
G14 interacting with rG$_0$ O2'	7.34 ± 2.26	5.13 ± 1.67
G6 aromatic stacking to rG$_0$	12.22 ± 2.24	6.15 ± 1.47

[1]metal ion-binding site II
[2]in percent of all MD simulation time ± SEM

Extended Data Fig. 10 | See next page for caption.

Extended Data Fig. 10 | Time-resolved atomic-level insights into the catalysis reaction. a) Series of 1D ^{1}H spectra recorded after addition of Mg^{2+} to pre-formed non-stabilized Dz^{5C}–RNA complexes revealing clear time-dependent changes of the peak intensities. b) Extract of 1D spectra recorded on Dz^{5C}–RNA before (black), directly after (blue), and at indicated time points (up to about 2 h) after Mg^{2+} addition. A spectrum recorded on stabilized Dz^{5C}–RNA^{2F}, preincubated with Mg^{2+} for three days, serves as a reference for the Mg^{2+}-equilibrated precatalytic complex (red). c) Contour plot of time-resolved 1D NMR data following the cleavage reaction. A magnification of data shown in (a) highlighting two peaks representing the educt (right) and product (left) state is displayed. A clear shift of the peak maximum during the initial stage of the reaction is apparent for the educt state, which is not present for the product state (dashed lines are given as guides). The direction of the observed frequency change follows the CSP induced by Mg^{2+} binding (visible in (b)) and therefore is in line with an increasing effective Mg^{2+}:Dz ratio. The data strongly suggest that the post-catalytic complex has a lower affinity for Mg^{2+} ions than the precatalytic complex leading to an effective Mg^{2+} release before product release. d,e) Series of 2D [^{1}H-^{1}H] TOCSY spectra recorded before (black) and successively after adding 1 mM $MgCl_2$. The acquisition time of each spectrum was 3 h. Clear peak position, peak shape, and/or intensity changes are present between the first (d, cyan) and second spectrum (e, brown). Only very weak intensity changes are present between second and third spectrum (e, orange). Indicated magnifications compare peak positions before (black) and during Mg^{2+}-induced transition (d, cyan/blue denote positive/negative contour levels) and after full cleavage (e, orange). f) Magnification of signal for rU_{+6} shown in (d). The peak positions from the Mg^{2+} titration obtained on Dz^{5C}–RNA^{2F} at indicated Mg^{2+} concentrations are shown as purple dashed lines. The regions representing the educt and product peaks in the real-time spectrum are highlighted in brown and orange. The region of the Mg^{2+}-free state is highlighted in grey. The data reveal that the observed transition does not start from the Mg^{2+}-free state but instead from a state that matches the frequencies of the Mg^{2+}-equilibrated state at Mg^{2+} levels between 0.5 and 1 mM. g) Overlay of time-resolved experimental data for one cross peak (T8-H6/H7; positive/negative contours are denoted in blue/cyan, respectively) with best-fit simulated spectrum (red/yellow denote positive/negative contours). Characteristic features of the initial and final states are indicated. The simulations can reproduce the experimental data well. Note that data shown in panels a, b, d and g show enlarged versions of the respective data shown in Fig. 3. h) Difference between experimental and simulated real-time NMR data as a function of different rate constants applied in the simulations. Results are shown individually for each resolved atom. The minimum represents the best fit condition. The nuclei can be divided into two groups, which either show rates that are slower than the FRET rate determined under matching conditions (brown dashed line) and are plotted in blue, or faster rates (plotted in red). Respective nucleotides are mapped on the structure in Fig. 3d) 1D slice of T8(H6-H7) obtained from the indirect dimension of the 2D spectrum recorded during the cleavage reaction (d, cyan). Experimental data (black, representing state C_1) is compared to peak shapes simulated using either a 2-state transition model (blue) or a 3-state transition model (red). Both simulated spectra represent the best fit for the respective model. Note that negative shoulders are better represented by the 3-state model (dotted arrows). j) Difference between the experimentally obtained data for indicated nucleotides and the simulated data as a function of the rate constant used in the simulation. While for dC_{+5} (grey) the overall fit is close to the experimental data (as visible by the rather low overall values of the difference), the peak is insensitive to changes in the rate constants (as visible by the low variations over the range of applied rate constants). The respective peak, therefore, is not a good sensor of the transition kinetics and was excluded from data interpretation. On the contrary, the data for C3 show a clear minimum and display good sensitivity in respect to changes in rate constants. The respective peak was therefore included in further data analysis. k) Likelihood of interactions of G14 or hexa-hydrated Mg^{2+} with the O2′ atom of rG_0 or the O5′ atom of rU_{-1} at the RNA cleavage site, when in any conformation of the cleavage site (left) and when the cleavage site is in the in-line attack conformation (angle O2′-P-O5′: 130–180°, right). An interaction is considered present if a hetero-atom of G14 or Mg^{2+} is within 5 Å of the target atom. l) Effect of Mg^{2+} binding to the metal ion-binding site II on the frequency of structural features of the RNA cleavage reaction during MD simulations at 20 mM Mg^{2+}. m) FRET-based activity assay in the presence of Mg^{2+} (red data points, 1 mM) or Mn^{2+} (blue data points, 0.5 mM) of Dz^{5C} with a 6-thio-modification at either G14 (left) or at G6 (right). While the measured behaviour of 6-thio-G6 is well in line with previous reports[23], the unusual behaviour of 6-thio-G14 would be in line with the acid-base mechanism shown in panel k (right, X_1 = G14).

nature research

Corresponding author(s): Manuel Etzkorn

Last updated by author(s): Oct 20, 2021

Reporting Summary

Nature Research wishes to improve the reproducibility of the work that we publish. This form provides structure for consistency and transparency in reporting. For further information on Nature Research policies, see our Editorial Policies and the Editorial Policy Checklist.

Statistics

For all statistical analyses, confirm that the following items are present in the figure legend, table legend, main text, or Methods section.

n/a	Confirmed
☐	☒ The exact sample size (*n*) for each experimental group/condition, given as a discrete number and unit of measurement
☐	☒ A statement on whether measurements were taken from distinct samples or whether the same sample was measured repeatedly
☒	☐ The statistical test(s) used AND whether they are one- or two-sided *Only common tests should be described solely by name; describe more complex techniques in the Methods section.*
☒	☐ A description of all covariates tested
☒	☐ A description of any assumptions or corrections, such as tests of normality and adjustment for multiple comparisons
☐	☒ A full description of the statistical parameters including central tendency (e.g. means) or other basic estimates (e.g. regression coefficient) AND variation (e.g. standard deviation) or associated estimates of uncertainty (e.g. confidence intervals)
☒	☐ For null hypothesis testing, the test statistic (e.g. *F*, *t*, *r*) with confidence intervals, effect sizes, degrees of freedom and *P* value noted *Give P values as exact values whenever suitable.*
☒	☐ For Bayesian analysis, information on the choice of priors and Markov chain Monte Carlo settings
☒	☐ For hierarchical and complex designs, identification of the appropriate level for tests and full reporting of outcomes
☒	☐ Estimates of effect sizes (e.g. Cohen's *d*, Pearson's *r*), indicating how they were calculated

Our web collection on statistics for biologists contains articles on many of the points above.

Software and code

Policy information about availability of computer code

Data collection	Topspin 3.2 and 4.0.6, AMBER19
Data analysis	Cara 1.9.1.5, Tospin 3.2 and 4.0.6, NMRpipe 8.9, Matlab2019a (including the matNMR 3.9.144 package)., Pymol-2.3.4, Origin 9.0G, Redcat, Xplor-NIH 2.49, eNORA, Sparky 3.114

For manuscripts utilizing custom algorithms or software that are central to the research but not yet described in published literature, software must be made available to editors and reviewers. We strongly encourage code deposition in a community repository (e.g. GitHub). See the Nature Research guidelines for submitting code & software for further information.

Data

Policy information about availability of data

All manuscripts must include a data availability statement. This statement should provide the following information, where applicable:

- Accession codes, unique identifiers, or web links for publicly available datasets
- A list of figures that have associated raw data
- A description of any restrictions on data availability

NMR resonance assignments of Dz5C·RNA2'F are available via the BMRB with accession code: 34654. Atomic coordinates of the Dz5C·RNA2'F ensemble (cluster I) are deposited in the PDB under accession code: 7PDU. Coordinates of additional cluster and scripts for data analysis are available from the corresponding author upon reasonable request.

Field-specific reporting

Please select the one below that is the best fit for your research. If you are not sure, read the appropriate sections before making your selection.

☒ Life sciences ☐ Behavioural & social sciences ☐ Ecological, evolutionary & environmental sciences

For a reference copy of the document with all sections, see nature.com/documents/nr-reporting-summary-flat.pdf

Life sciences study design

All studies must disclose on these points even when the disclosure is negative.

Sample size	For NMR data acquisition, individual samples for each condition were used relaying on the intrinsic ensemble averaging of the method. Sample stability was assessed for all conditions via characteristic spectral properties. Sample reproducibility was explicitly checked via different sample preparations. For mutation studies all possible (natural) nucleotide substitutions were used at all individually tested positions. The EPR experiments focused on the condition representing the central element of the study. Additional conditions have been reported before (ref. 20). For MD simulations 10 independent runs for each condition were computed to ensure sufficient sampling space and assess reproducibility.
Data exclusions	Only NMR peaks with unresolved signal overlap where excluded from analysis.
Replication	Key samples for NMR were tested by preparation with different stocks at different days showing high reproducibility of NMR spectra. Time-resolved 1D NMR results were repeated in two independent experiments. Cross validation of NMR data was carried out by analysis of the total observed spectral changes, which agree well with the respective kinetics observed via FRET. The same behavior was also detected in the 2D NMR measurement series confirming reproducibility of the experimental setup. Reproducibility of used kinetic assays was previously confirmed (ref. 20). EPR measurements of selected conditions were repeated at different days using independent sample preparations confirmed high reproducibility of EPR read out parameters. Activity of mutations were determined in triplicates. In general, all attempts at replication were successful including NMR, EPR, FRET, and PAGE data.
Randomization	No experimental design that required randomization was used in our study.
Blinding	Blinding was not used since it was not feasible (experimental design, data acquisition, and analysis required expertise of same highly trained researcher, i.e., for NMR, EPR, and MD experiments) and/or not relevant for the experimental design (in vitro activity assays). Instead, all data interpretation resulted from objective data analysis consistently involving all acquired data points.

Reporting for specific materials, systems and methods

We require information from authors about some types of materials, experimental systems and methods used in many studies. Here, indicate whether each material, system or method listed is relevant to your study. If you are not sure if a list item applies to your research, read the appropriate section before selecting a response.

Materials & experimental systems

n/a	Involved in the study
☒	☐ Antibodies
☒	☐ Eukaryotic cell lines
☒	☐ Palaeontology and archaeology
☒	☐ Animals and other organisms
☒	☐ Human research participants
☒	☐ Clinical data
☒	☐ Dual use research of concern

Methods

n/a	Involved in the study
☒	☐ ChIP-seq
☒	☐ Flow cytometry
☒	☐ MRI-based neuroimaging